Nanoscale
Advances

ROYAL SOCIETY
OF CHEMISTRY

PAPER

View Article Online
View Journal

Check for updates

Cite this: DOI: 10.1039/d6na00263c

Titanium dioxide nanotubes modified with nickel oxide and nickel nanoparticles for improved polysulfide anchoring and redox kinetics in lithium–sulfur batteries

Emmanuel Siaw,[ab] Dias Bekeshov,[ab] Alas Alaskhanov,[ab] Aishuak Konarov,[a] Zhumabay Bakenov,[ac] Nurzhan Baikalov*[b] and Stavros G. Poulopoulos*[ab]

Received 4th April 2026
Accepted 30th May 2026

DOI: 10.1039/d6na00263c

rsc.li/nanoscale-advances

This study systematically investigates and compares the roles of electronic conductivity, polysulfide chemisorption, and catalytic conversion in TiO_2 nanotube-based cathode hosts by evaluating three bifunctional additives: bare TiO_2 nanotubes, NiO-modified TiO_2 nanotubes (NiO/TiO_2), and Ni nanoparticle-modified TiO_2 nanotubes (Ni/TiO_2). Anatase phase TiO_2 nanotubes (~18.3 nm) were synthesized *via* a hydrothermal method and integrated into carbon fibre paper to form TiO_2-CFP, NiO/TiO_2-CFP and Ni/TiO_2-CFP composite cathodes, which were evaluated at a high sulfur loading of 4 mg cm^{-2}. The cell with TiO_2-CFP exhibited moderate polysulfide adsorption but was constrained by poor conductivity and weak catalytic activity, delivering an initial capacity of 995.72 mA h g^{-1} at 0.2C. The cell with NiO/TiO_2 improved chemisorption and redox conversion, achieving an initial capacity of 1196.4 mA h g^{-1} at 0.2C. Among the tested electrodes, Ni/TiO_2-CFP delivered the best overall performance, exhibiting an initial specific capacity of 1285 mA h g^{-1} at 0.2C and retaining ~1095 mA h g^{-1} after 100 cycles. Moreover, it showed excellent rate capability: 745.25 mA h g^{-1}, 659.03 mA h g^{-1}, and 381.52 mA h g^{-1} at 0.5C, 1.0C and 2.0C, respectively, significantly outperforming cells with TiO_2-CFP and NiO/TiO_2-CFP. Ni/TiO_2-CFP further exhibited distinct charge–discharge plateaus with minimal polarization, the lowest charge transfer resistance (14 Ω) and the highest Li_2S nucleation capacity (746 mA h g^{-1}), confirming faster interfacial kinetics. These results establish that the metallic Ni modification of TiO_2 nanotubes most effectively balances polysulfide anchoring and catalytic conversion, providing a rational design pathway for high-loading Li–S battery cathodes.

1 Introduction

The development of lithium-ion batteries (LIBs) has been crucial for the rise of modern, portable technology and electric mobility.[1,2] Generally, LIBs utilize cathode materials including intercalation-type transition metal oxides and phosphates. However, these materials inevitably limit the energy density of LIBs to below 400 W h kg^{-1}, a level that is not high enough for applications involving high energy storage requirements, such as grid-scale applications,[3] electric vehicles,[4] and advanced portable electronics.[5,6] Beyond energy limitations, the hazard potential and high cost of these cathode materials also underscore the paramount importance of new battery chemistries that are less hazardous, more environmentally friendly, and economically viable.[7] Recent research continues to highlight these constraints, confirming that surpassing the intrinsic energy density limitations of conventional LIBs remains one of the most pressing challenges in modern energy storage.[8] Therefore, it becomes crucial to investigate alternative battery materials that can meet the high demands of advanced technology while minimizing environmental harm.

Li–S batteries are seen to be among the most promising options for energy storage because of their high theoretical capacity, which is due to the redox reactions that occur between lithium and sulfur to form lithium sulfide ($16\ \text{Li} + S_8 = 8\ Li_2S$).[9,10] Despite the benefits of low cost, abundance, and low toxicity, sulfur's poor conductivity, massive volume growth during cycling, and dissolution of intermediate lithium polysulfide species (LiPSs) hinder the development of Li–S batteries.[11–14] A 2025 review underscored that despite significant recent progress, a substantial gap between fundamental Li–S research and practical commercialization persists, driven by slow cathode kinetics, electrolyte instability and anode interface challenges.[15] Similarly, Fei and Li highlighted that low sulfur

---

[a] Department of Chemical and Materials Engineering, Nazarbayev University, Astana 010000, Kazakhstan. E-mail: nurzhan.baikalov@nu.edu.kz; stavros.poulopoulos@nu.edu.kz

[b] National Laboratory Astana, Nazarbayev University, Astana 010000, Kazakhstan

[c] Institute of New Materials and Energy Technologies, Nazarbayev University, 010000, Astana, Kazakhstan

loading, excessive electrolyte use and an unlimited cathode sulfur fraction continue to significantly constrain the practical energy density of Li–S batteries.[16] Hence, numerous host materials, such as carbon materials,[17,18] conductive polymers,[19] metals,[20,21] *etc.*, have been proposed to date to improve the performance of Li–S batteries. Carbon materials are frequently employed as host materials for Li–S batteries because of their strong electrical conductivity and tunable pore structure.[22] Nevertheless, the nonpolar carbon material is physically unable to bind to polar LiPSs, which pass through the separator and reach the anode, causing an irreversible capacity loss during battery cycling; this phenomenon is known as the shuttle effect. The shuttle effect can be efficiently suppressed by using polar materials such as metal oxides,[23,24] metal sulfides,[25,26] metal carbides[27,28] and metal nitrides[29,30] based on Lewis's acid–base interaction or surface redox. Among these metal oxides, TiO_2 is a wide bandgap (3.2 eV) n-type semiconductor material,[31,32] which has been extensively reported as a promising electrode material for Li–S batteries.[33–35] Since interfacial phenomena (that is, the interactions occurring at the contact interface between LiPSs and host materials) play a key role in determining chemical interactions and affinities,[33] various structures with large specific surface areas, such as hollow nanosheets,[36] nanospheres,[37] nanoparticles,[38] and nanotubes,[39] have been developed to improve interfacial reactions.[40]

Multiple TiO_2 morphologies have been studied and have shown promise, with TiO_2 nanotubes attracting particular attention.[41–44] TiO_2 nanotubes typically exhibit high specific surface areas, tunable tube or pore diameters in the tens of nanometers, and an open tubular architecture that promotes efficient electrolyte penetration and interfacial accessibility.[45,46] Recent developments in heterostructured systems, including anatase/bronze TiO_2 coupled with polypyrrole and TiO_2/GO-coated functional separators, have improved LiPS confinement and cycling stability in Li–S batteries.[47,48] More recently, TiO_2 nanotubes loaded with WS_2/MoS_2 heterostructures have been shown to construct adsorption–diffusion conversion channels for LiPSs, achieving strong cycling performance under sulfur loadings as high as 5.8 mg cm^{-2}, further demonstrating the promise of TiO_2 nanotube-based systems while simultaneously reinforcing that intrinsic conductivity limitations remain the central unresolved challenge.[39] Despite advances in TiO_2-based structures for LiPS control and structural stability, the practical application of TiO_2 remains constrained by its intrinsically low electronic conductivity. For pristine anatase TiO_2, a room-temperature resistivity of approximately 10^{12} Ω cm, corresponding to a conductivity of approximately 10^{-12} S cm^{-1}, has been reported.[49]

To overcome the poor conductivity of TiO_2 while preserving its strong polysulfide-binding ability, several material modification strategies have been explored.[50–54] For instance, Pu *et al.* reported that Ru nanocluster-modified TiO_2 nanotubes created an active TiO_2 and Ru heterointerface that enhanced LiP adsorption and accelerated conversion kinetics and improved the cycling stability of Li–S batteries. Nickel nanoparticles have emerged as a particularly promising material due to their multifunctional properties in Li–S battery systems.[53] Moreover, a niobium nanoparticle catalyst loaded on TiO_2 nanotubes, according to Barlow *et al.*, exhibits the combined effects of chemical adsorption, physical confinement, and catalytic conversion of polysulfides.[54] The natural polarity of TiO_2 and the similar ionic diameters of titanium and niobium, which result in numerous defects that enhance electrical conductivity and catalytic activity, facilitate catalyst infiltration into the TiO_2 lattice, leading to a three-dimensional hierarchical structure that effectively mitigates the polysulfide shuttle effect while accelerating conversion kinetics.[54]

As nickel nanoparticles are added to metal oxide-based hosts in Li–S batteries, they give a boost to the catalytic and electrical conductivity of these materials. The interaction of nickel with the oxide host also helps to strongly anchor polysulfides to the cathode and promotes faster electron and ion transport.[55] Supporting this, a recent study demonstrated that Ni/NiO-embedded carbon nanofibers effectively reduced the polarization of Li–S, accelerated LiPS conversion kinetics, and improved active material utilization by leveraging the dual functionality of metallic Ni domains and NiO redox sites, validating the complementary role that Ni and NiO play when combined in a single host system.[56] Moreover, NiO exhibits complementary functionality: abundant redox-active Ni^{2+}/Ni^{3+} sites for catalytic conversion of polysulfides, strong polysulfide binding (∼1.2 eV for Li_2S_4), and electrical conductivity several orders of magnitude higher than TiO_2 (10^{-3} to 10^{-1} S cm^{-1}), depending on defect concentration.[57] In addition, the reduction of NiO nanoparticles forms metallic Ni domains, creating efficient electron transport pathways that enhance the system's conductivity and overall electrochemical performance.[55] Nickel-based composites with strong chemical trapping ability and multiple oxidation states have indeed shown significant promise for catalyzing LiPS conversion and inhibiting the shuttle effect in diverse host configurations.[58]

Although TiO_2-based polysulfide trapping materials for Li–S batteries have been widely studied, direct comparisons of TiO_2 nanotubes, TiO_2 nanotubes modified with NiO, and TiO_2 nanotubes modified with Ni nanoparticles incorporated into carbon fibre paper remain limited. Moreover, despite growing recognition of the distinct but complementary roles of NiO and metallic Ni in polysulfide management, a systematic evaluation of these three cathode architectures under identical high sulfur loading conditions has also not been reported. As a result, their respective influence on polysulfide anchoring and redox kinetics has not yet been clearly established.

In this study, three anatase phase TiO_2 nanotube-based additives with an average nanotube diameter of approximately 18.3 nm were synthesized *via* a hydrothermal method. These materials were engineered as bifunctional additives to simultaneously anchor lithium polysulfides and catalyze their conversion at a high sulfur loading. For practical electrochemical evaluation, they were integrated into carbon fibre paper matrices to form composite cathodes, TiO_2-CFP, NiO/TiO_2-CFP, and Ni/TiO_2-CFP. Although the cell with TiO_2-CFP exhibited moderate polysulfide adsorption, its effectiveness was restricted by poor electrical conductivity and weak catalytic activity. By comparison, the cell with NiO/TiO_2-CFP exhibited enhanced chemisorption and facilitated redox conversion, whereas the cell with Ni/TiO_2-CFP markedly improved conductivity and accelerated lithium polysulfide reaction kinetics, leading to improved electrochemical performance in lithium–sulfur batteries. By directly comparing these three cathode systems under identical conditions at high sulfur loading, this study provides mechanistic clarity on the interplay between polysulfide anchoring, catalytic conversion, and electronic conductivity in TiO_2-based hosts, insights essential for guiding the rational design of next-generation Li–S battery cathodes towards practical energy density targets.

2 Experimental section

2.1 Preparation of TiO_2 nanotubes decorated with nickel oxide/nickel nanoparticles

Titanium(IV) dioxide (99.7% Sigma-Aldrich) nanotubes were synthesized by a one-step hydrothermal templating process.[59] In brief, 1.5 g of anatase TiO_2 powder (99.7%, Sigma-Aldrich, USA) was added to 100 ml of 10 M sodium hydroxide (NaOH, ≥98% Sigma-Aldrich) under magnetic stirring for 12 hours to produce a uniform solution. The solution was transferred to a 100 ml Teflon autoclave and heated at 130 °C in a muffle furnace for 24 hours. After cooling to room temperature, the resulting precipitate was collected *via* centrifugation. The precipitate was then washed several times with 0.5 M hydrochloric acid (HCl, 38%, Sigma-Aldrich) and deionized water until a neutral pH was achieved. Finally, the product (TiO_2 nanotubes) was air-dried in an oven at 60 °C overnight. The TiO_2 nanotubes in powder form were then calcined in a muffle furnace at 600 °C for 2 hours to improve crystallinity. Reaction temperature and time were found to influence the nanotube structure, wall thickness, and tube length. For surface decoration, 0.11 g of nickel(II) nitrate hexahydrate (Ni $(NO_3)_2\cdot 6H_2O$ ≥97% Sigma-Aldrich, USA) was dissolved in 1.1 ml of deionized water and an alkaline polyethylene glycol (PEG) solution was prepared by dissolving 20 mg of PEG ($MW = 10\,000$ g mol^{-1}, Sigma-Aldrich, Germany) in 50 ml deionized water, followed by adjustment of the alkalinity with NaOH to a final concentration of 50 mM. Subsequently, 0.3 g of synthesized TiO_2 nanotubes was added dropwise to the alkaline PEG solution. The solution was then stirred vigorously (1000 rpm) for 300 seconds at room temperature. The light-green precipitate was filtered and washed several times with deionized water and ethanol. Finally, the product (NiO/TiO_2) formed was air-dried at 50 °C for 24 hours. After calcination at 450 °C for 2 hours, NiO/TiO_2 nanotubes in powder form were synthesized with a TiO_2 to NiO molar ratio of 10 : 1.[60] To synthesize Ni/TiO_2, the NiO/TiO_2 powders were reduced in a N_2/H_2 atmosphere for 2 hours at 450 °C to produce TiO_2 nanotubes decorated with metallic Ni nanoparticles. The sample was cooled under inert conditions to avoid re-oxidation. Reaction time and temperature, along with molar ratios, were effectively regulated to tailor the structural and functional properties of the material. Fig. 1a illustrates the steps involved in the synthesis of TiO_2 nanotubes. The resulting nanotubes were subsequently decorated with NiO and Ni nanoparticles, as shown in Fig. 1b.

2.2 Preparation of cathode materials

During the preparation of the slurry, 30 mg of TiO_2-based nanotubes, 20 mg of acetylene black (MTI Corporation, USA), 130 mg of carbon nanotubes (CNTs, ISOLAB, Germany) and 20 mg of polyvinylidene fluoride (PVDF, Sigma-Aldrich, France) were dispersed in 3.5 ml of *N*-methyl-2-pyrrolidone (NMP, ≥99%, Sigma-Aldrich, USA) using a high speed Thinky mixer. The prepared slurry was then cast on carbon fibre paper (current collector) to create cathodes for the cells. To ensure uniform dispersion, the mixture was homogenized for 300 seconds at 1200 rpm. An active material loading per disc was obtained by drop-casting approximately 30 μl of the slurry onto carbon fibre paper. Before use, the electrodes were dried in a vacuum oven at 70 °C for 24 hours.

2.3 Cell assembly

Using the prepared TiO_2-based cathodes, Celgard® 2500 as the separator, and a lithium chip as the anode, CR2032 coin cells were assembled in an MBRAUN argon-filled glovebox (H_2O < 0.1 ppm, O_2 < 0.1 ppm). After applying the polysulfide solution (catholyte) to the dried electrode, the electrolyte (1 M LiTFSI with 2 wt% $LiNO_3$ in DOL/DME, 1 : 1 v/v) was added. An additional amount of electrolyte was added to the anode side of the separator. A lithium chip, a spacer and a wavy spring were added to the cell stack, and the cell was sealed using a manual hydraulic crimper under a pressure of 100 kg cm^{-2}.

2.4 Materials characterization

The structure and morphological parameters of the synthesized materials were investigated using a scanning electron microscope (SEM), namely JEOL JSM-IT800, Japan, with Energy Dispersive X-ray Spectroscopy (EDS) and Cs-Corrected Scanning Transmission Electron Microscopy (JEOL(JEM-ARM200F)). X-ray diffraction (XRD, Rigaku SmartLab, Japan) in the angle range of 2θ between 10° and 90° was used for establishing the crystalline phase composition using Cu Kα radiation (λ = 1.54056 Å). Thermogravimetric analysis (TGA; an STA 449 F5 Jupiter coupled to a QMS 403 Aeolos Quadro, Germany) was employed to investigate the thermal behaviour of TiO_2, NiO/TiO_2, and Ni/TiO_2 nanotubes in powder form. This analysis was carried out by thermogravimetric analysis using a simultaneous thermal analyzer under argon gas (240.3 ml min^{-1}) from 25 to 650 °C at a rate of 5 K min^{-1}. Textural parameters, *i.e.*, specific surface area and pore volume, were investigated based on nitrogen adsorption–desorption isotherms (Micromeritics TriStar II Plus, England) and pore size distribution determined by the Barrett–Joyner–Halenda (BJH) method. X-ray photoelectron spectroscopy (XPS, NEXSA, Thermo Scientific, USA) was employed for examining oxidation state changes and interactions with LiPS. Elemental composition and metal loading by metal oxide composites were also investigated by inductively coupled plasma optical emission spectroscopy (ICP-OES, iCAP 6300-Thermo Scientific, England).

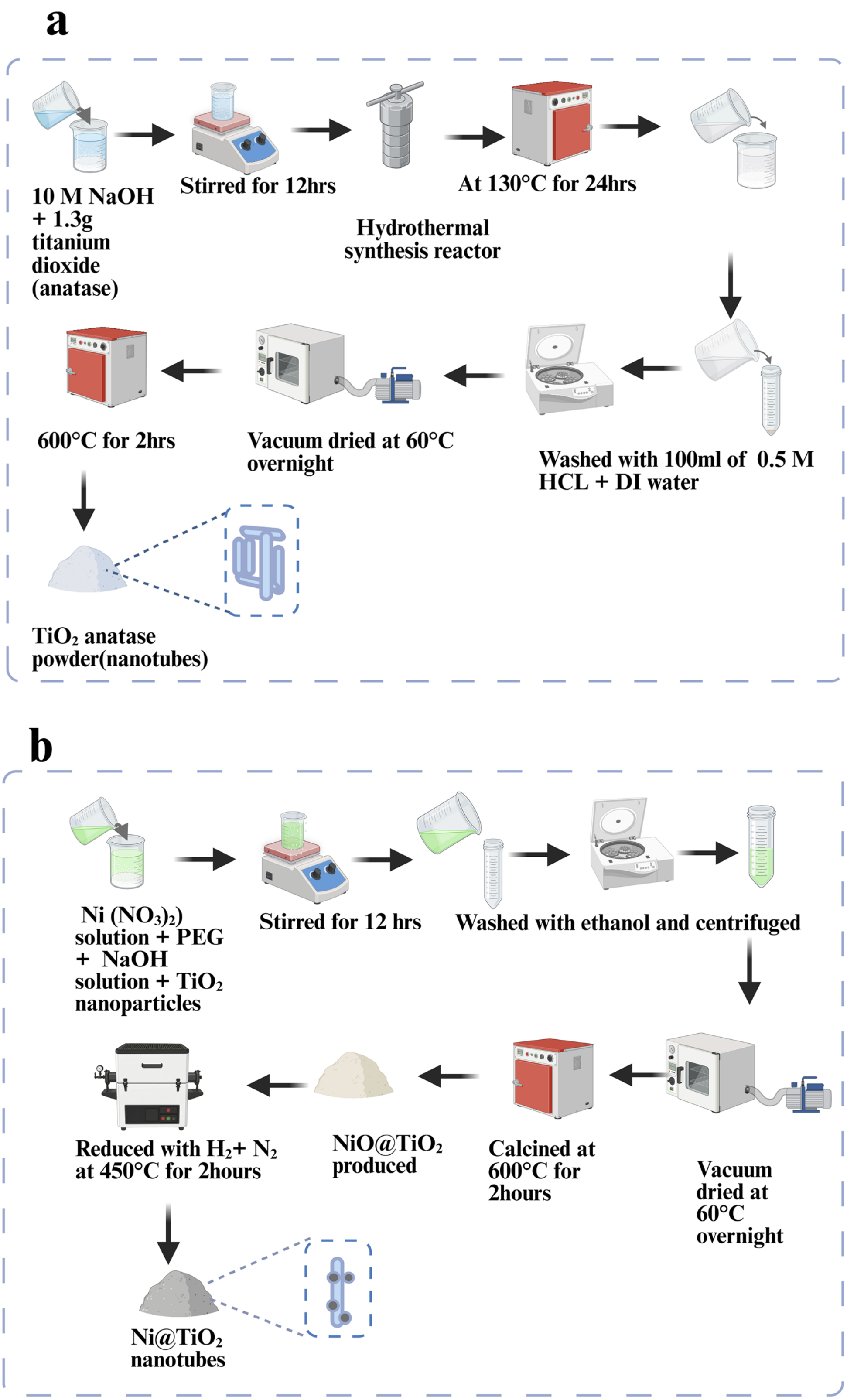

Fig. 1 Schematic illustration depicting the synthesis route of (a) TiO_2 nanotubes and (b) decoration of NiO and Ni nanoparticles on the nanotubes. (b) Created with Biorender.com.

2.5 Electrochemical characterization

Lithium metal was employed as the counter/reference electrode, with a 1 M Li_2S_6 solution serving as the catholyte and carbon fibre paper, CFP, serving as the cathode current collector. Carbon-coated separators were used for the assembly of the Li–S coin cells. For the two loading scenarios, 11.8 μL and

23.5 μL of Li_2S_6 were added, corresponding to sulfur loadings of 2.0 and 4.0 mg cm^{-2}, respectively. A strict electrolyte-to-sulfur, E/S, ratio of 10 : 1 was maintained by adding an additional electrolyte volume of 10.8 μL for the 2.0 mg cm^{-2} cell and 21.7 μL for the 4.0 mg cm^{-2} cell to the anode side. The electrolyte consisted of 1 M LiTFSI with 2% wt $LiNO_3$ in a 1 : 1 (v/v) mixture of DOL and DME. Galvanostatic charge–discharge measurements were performed using a Neware battery testing system within a voltage window of 1.7–2.8 V *vs.* Li/Li^+. Cyclic voltammetry (CV) analyses were performed on a Biologic VMP3 potentiostat/galvanostat within the same potential range, while electrochemical impedance spectroscopy (EIS) was performed at an amplitude of 5 mV over a frequency range of 100 kHz to 1 MHz. The areal sulfur mass loading (s_m) was calculated using the following expression:

$$s_m = \frac{m_s}{A} = \frac{V \times C \times n \times M_s}{A};$$

where s_m – the areal sulfur mass loading (mg cm^{-2}), m_s – the sulfur mass on the CFP mat (mg), V – the catholyte volume (L), A – the CFP mat area (cm^2), C – the Li_2S_6 molar concentration (mol L^{-1}), n – the number of sulfur atoms (for Li_2S_6, $n = 6$), and M_S – relative atomic mass of sulfur (32 g mol^{-1}).[61]

2.6 Lithium polysulfide binding analysis

The chemical binding behaviour of LiPS was assessed *via* the Ti 2p, Ni 2p, O 1s, and S 2p regions on the XPS spectra obtained from ($Ø = 16$ mm) CFP, TiO_2-CFP, NiO/TiO_2-CFP, and Ni/TiO_2-CFP electrodes. These electrodes were soaked in 2 ml of a 5 mM Li_2S_6 solution dissolved in 1,3-dioxolane and 1,2-dimethoxyethane (DOL/DME, $\nu = 1:1$) for 24 h. The test was then conducted at room temperature inside an MBRAUN glovebox (H_2O < 0.1 ppm and O_2 < 0.1 ppm) with a duration of 24 h. Afterwards, XPS analysis was performed on the CFP, TiO_2-CFP, NiO/TiO_2-CFP, and Ni/TiO_2-CFP electrodes, before and after soaking in the Li_2S_6 solution.

2.7 Symmetric cell test

Symmetric cells were constructed by employing two identical synthesized electrodes, separated by a Celgard® 2400 membrane. The catholyte was prepared as a 0.3 M Li_2S_6 solution in a 1 : 1 (v/v) DOL/DME solvent system, and 25 μl was added to both the cathode and the separator. The electrochemical behaviour of polysulfides was investigated by cyclic voltammetry (CV) on a Biologic VMP3 potentiostat/galvanostat at scan rates of 20, 10, and 1 mV s^{-1}, respectively, within a potential window of −1.0 V to 1.0 V (*vs.* Li/Li^+).

2.8 Nucleation test

The synthesized material was deposited on the electrode; thus, carbon fiber paper (CFP) served as the working electrode, while metallic lithium discs ($Ø = 16$ mm) functioned as both the counter and reference electrodes. A volume of 20 μl of 0.5 M Li_2S_6 solution in tetraglyme acted as the catholyte, whereas 20 μl of a 1 M lithium bis(trifluoromethanesulfonyl)imide (LiTFSI) solution containing 2 wt% $LiNO_3$ prepared in a 1 : 1 (v/v) DOL/DME solvent mixture served as the anolyte. CR2032 coin cells with TiO_2-CFP, NiO/TiO_2-CFP and Ni/TiO_2-CFP electrodes were assembled separately and discharged under constant current to 2.06 V, followed by a potentiostatic hold at 2.05 V until the current decreased below 1×10^{-5} A to induce Li_2S_6 nucleation.

2.9 Beaker cell test

All cathodes with their respective additives (TiO_2, NiO/TiO_2, and Ni/TiO_2) were tested for Li_2S_6 adsorption to determine their adsorption capacities. The cathodes (TiO_2-CFP, NiO/TiO_2-CFP and Ni/TiO_2-CFP) and anode (lithium-ion metal disc) were submerged in a 10 ml solution of 3 μM Li_2S_6 solution. Electrochemical behaviour was investigated by cyclic voltammetry (CV) on a Biologic VMP3 potentiostat/galvanostat at a scan rate of 1 mV s^{-1} within a potential window of −0.01 V to 0.01 V (*vs.* Li/Li^+). Three time intervals, 3, 6 and 12 h, were monitored to provide sufficient time for polysulfide adsorption, leading to an observable colour change.

3 Results and discussion

3.1 Physical characterization of TiO_2 nanotube-based samples

In Fig. 2a, X-ray diffraction analysis of respective samples confirmed the anatase phase of TiO_2, as evidenced by the distinctive peaks at $2\theta \approx 25.3°$, 37.8°, 48.0°, 55.1°, 63.1°, 70.9° and 75.4°, which can be assigned to the (101), (004), (200), (211), (204), (220), and (215) crystallographic planes corresponding to the anatase form of TiO_2 (JCPDS 21-1271).[40] In addition, NiO and Ni were identified by the characteristic (111) and (200) peaks near $2\theta \approx 44.5°$ and 43.3°, respectively.[62] Moreover, in Fig. 2b, thermogravimetric analysis (TGA) results revealed that all samples exhibited a small initial weight loss at approximately 120 °C, which was attributed to the desorption of physically adsorbed water. A gradual decrease in weight was then observed up to approximately 450 °C, corresponding to dehydroxylation and the decomposition of organic residues remaining from the synthesis route. The highest total weight loss was observed for the pure TiO_2 sample. Lower weight losses were observed for NiO/TiO_2 and Ni/TiO_2, indicating enhanced thermal stability, which may be attributed to Ni decoration. No significant weight loss was observed for any of the three samples between approximately 450 °C and approximately 650 °C. Hence, in this current study, the optimal calcination temperature was fixed at 450 °C based on the TGA curves. The pore size distribution of the material was analyzed using the Barrett–Joyner and Halenda (BJH) method. The samples were further examined using nitrogen adsorption–desorption isotherms (Fig. 2c), which exhibited a type IV profile with H3-type hysteresis in the relative pressure range of 0.4 to 0.9 P/P_o, confirming the presence of mesopores and slit-like pores. The sharper uptake near 0.9 P/P_o indicates filling of large mesopores and interparticle voids, with the nickel-containing sample showing higher adsorption capacity, suggesting larger pore volume and surface area.[63] The pore size distribution (Fig. 2d) shows that Ni/TiO_2 exhibits a dominant mesoporous structure

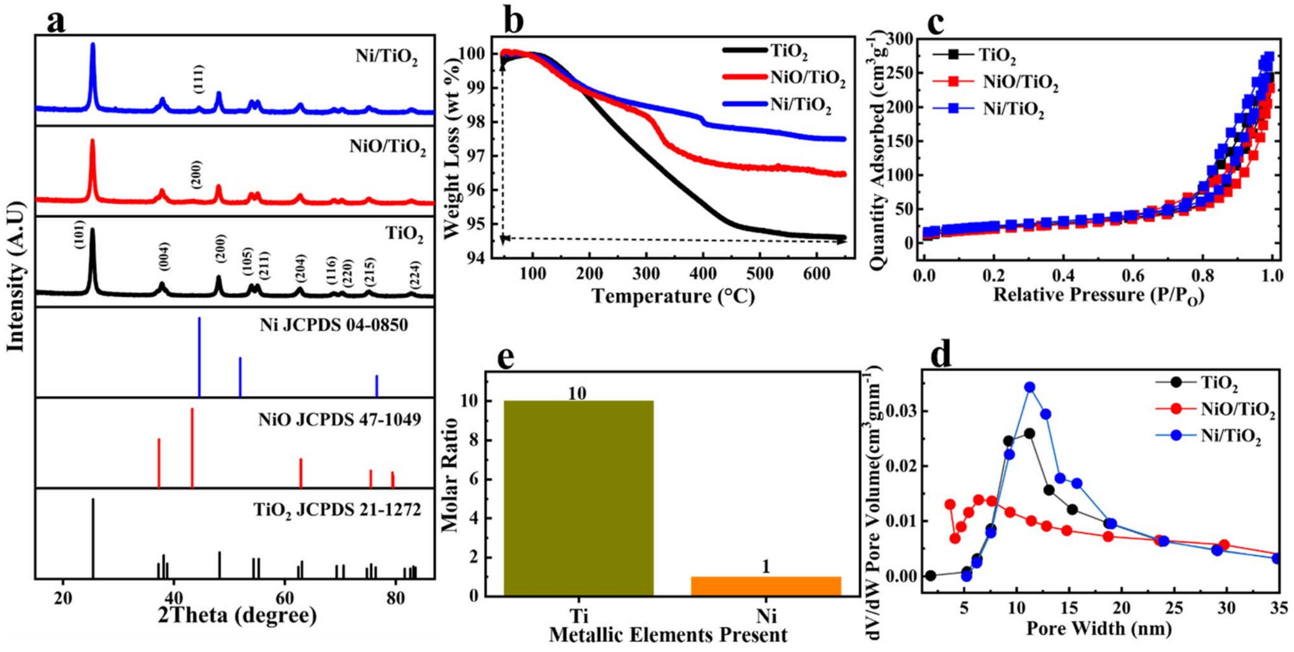

Fig. 2 Physical characterization of TiO_2, NiO/TiO_2, and Ni/TiO_2 nanotubes: (a) XRD pattern, (b) TGA, (c) nitrogen adsorption–desorption isotherms, (d) pore size distribution and (e) ICP OES.

(3–5 nm) with a higher pore volume than NiO/TiO_2 and pure TiO_2, making it more suitable for applications requiring a large surface area and efficient mass transport. ICP-OES analysis (Fig. 2e) indicated a Ti : Ni molar ratio of approximately 10 : 1, consistent with the ratio used during the synthesis. Table S1 also reports the BET surface areas of the respective samples, with Ni/TiO_2 exhibiting the largest surface area, 87.71 $m^2\ g^{-1}$. Moreover, the average particle size of nanotubes (Fig. S1) was determined to be 18.27 nm. Overall, the results confirm the successful formation of thermally stable, anatase-phase mesoporous Ni/TiO_2 nanotubes with an optimized composition, a large surface area, and a favourable pore structure.

Fig. 3 presents comprehensive morphological characterization of TiO_2 nanotubes and TiO_2 nanotubes modified with NiO/Ni nanoparticles using SEM and TEM imaging across multiple scales. Fig. 3a shows TiO_2 nanotubes with vertically aligned, smooth-walled tubular morphology, consistent with hydrothermal treatment-derived structures. These structures are known to offer a high surface area and facilitate ion transport. Fig. 3b reveals NiO/TiO_2 with a visibly roughened surface and granular texture, resembling agglomerated NiO, which may be due to calcination. In Fig. 3c, TiO_2 shows a discrete nanoparticle dispersion across the TiO_2 framework with slightly shorter lengths of the nanotube. Low-resolution TEM images of Ni/TiO_2 at 50 nm and 100 nm are shown in Fig. 3d and e, respectively, revealing aggregated nanostructures and confirming the decoration of Ni within the TiO_2 matrix. An additional surface morphological investigation was conducted using TEM, as seen in Fig. 3f. The interplanar spacing of the (101) plane of the TiO_2 anatase phase was determined to be approximately 0.35 nm. For Ni nanoparticles, the interplanar spacings of the (111) and (200) planes were found to be 0.203 nm and 0.176 nm, respectively.

Fig. 4(a–d) display Ni/TiO_2-CFP electrodes at increasing magnifications, revealing a hierarchically porous architecture with interconnected domain features and EDS maps indicating the presence of Ti and Ni, respectively. The purpose of this analysis was to determine the presence of TiO_2 nanotubes, NiO nanoparticles and Ni nanoparticles in the cathode material. Additionally, elemental mapping was performed to confirm the homogeneous distribution of these elements. It was observed that fragments were attached to single strands of carbon fibre in the cathode material, and each fragment was observed to contain Ti and Ni, as revealed by the EDS maps.

Systematic XPS characterization revealing the surface chemical changes through all stages of material modification is shown in Fig. S2. Survey spectra (Fig. S2a) indicate that carbon fibre paper (CFP) contains C 1s and O 1s signatures, which agree with the presence of graphitic carbon and surface oxidic functionalities.[64] The TiO_2-CFP survey spectrum shows the presence of Ti 2p and F 1s peaks, where the appearance of the fluorine signal arises from the polymer binder used in fabricating the electrodes. Moreover, the appearance of Ni 2p features in the spectra of the electrodes containing NiO/TiO_2 and Ni/TiO_2 confirms the presence of nickel in the composite material. C 1s spectra (Fig. S2b) indicate three discernible carbon environments in all samples: C–C (∼284.8 eV), C–O (∼286.0 eV), and O=C–O (∼288.5–289.0 eV) corresponding to sp^2 carbon, ether/alcohol functionalities, and oxidized carbon, respectively.[65,66] The reduction in C 1s intensity with increasing surface coverage from CFP through the metal-decorated samples correlates with increasing TiO_2 and nickel coverage. Ni 2p spectra (Fig. S2c and f) distinguish nickel oxidation states. NiO/TiO_2-CFP presents a Ni $2p_{3/2}$ peak at ∼856 eV and a Ni $2p_{1/2}$ peak at ∼873.5 eV with high-intensity satellite bands, typical of Ni^{2+} in NiO. In contrast,

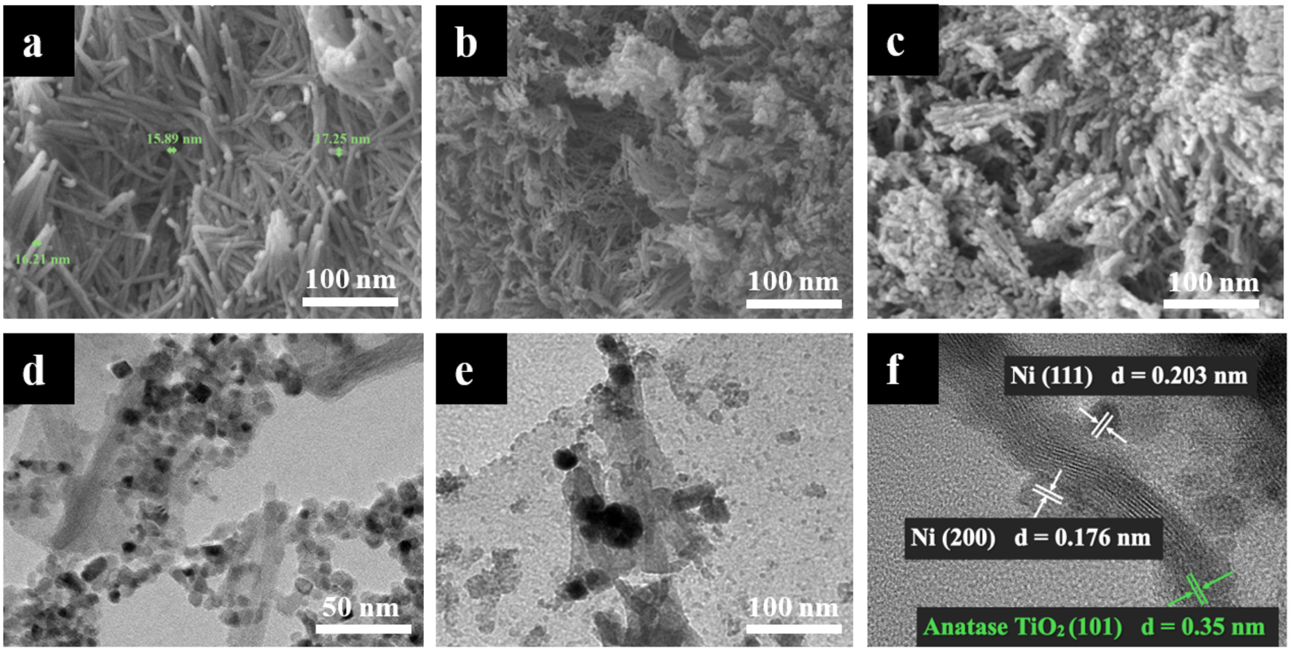

Fig. 3 SEM images of nanotubes: (a) TiO_2, (b) NiO/TiO_2, and (c) Ni/TiO_2; low-resolution TEM image of Ni/TiO_2 nanotubes at (d) 50 nm and (e) 100 nm; and (f) HRTEM images of Ni/TiO_2 (*d*-spacing).

Ni/TiO_2-CFP displays peaks at 852.8 eV and 857 eV, which correspond to Ni^{2+} and Ni^{3+}, respectively.[40,56] The O 1s spectra (Fig. S2d) show three components, including lattice oxygen (Ti–O) at ∼530.0 eV, surface hydroxyls (Ti–OH) at ∼531.5 eV, and surface species at ∼533.0 eV, consistent with TiO_2 surface chemistry.[54] Ti 2p spectra (Fig. S3e) show a 2p doublet, namely Ti $2p_{3/2}$ at ∼458.5 eV and Ti $2p_{1/2}$ at ∼464.5 eV with ∼5.5 eV splitting, which confirms the Ti^{4+} oxidation state.[67–69] The XPS results validate the structural and chemical integrity of the materials before exposure to Li_2S_6 by confirming the presence of well-defined nickel and titanium oxidation states.

XPS characterization following Li_2S_6 soaking, as shown in Fig. 5 and S3, presents the polysulfide adsorption tendency along with chemical interactions in all the composite materials.

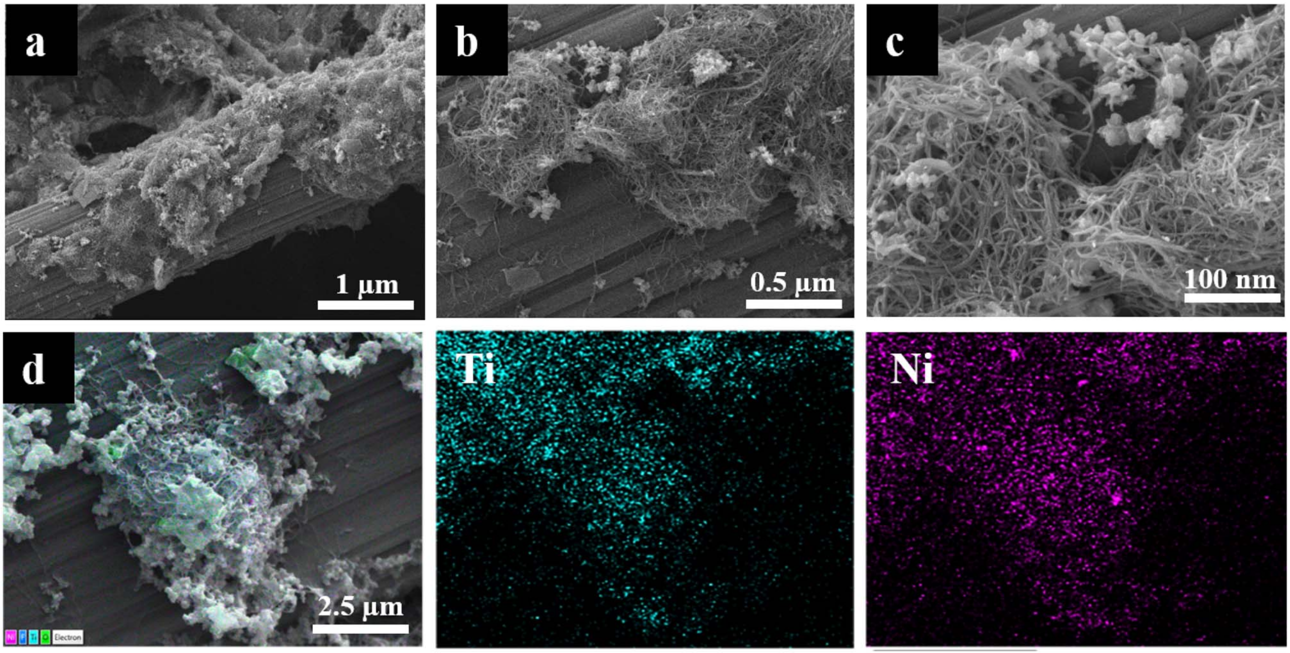

Fig. 4 SEM image of the Ni/TiO_2-CFP electrode at (a) 1 µm, (b) 0.5 µm, and (c) 100 nm; EDS maps of the Ni/TiO_2 electrode at (d) 2.5 µm.

Survey spectra (Fig. S3a) show that all electrodes (CFP, TiO_2-CFP, NiO/TiO_2-CFP, and Ni/TiO_2-CFP) show a distinct S 2p peak following Li_2S_6 exposure, verifying the successful polysulfide adsorption, with the accompanying retention of their intrinsic characteristic elemental signatures of C 1s, O 1s, and metal peaks (Ti 2p, Ni 2p, and F 1s where applicable). C 1s spectra (Fig. S3b) indicate that CFP after soaking has three carbon environments with C–C bonds at ∼284.8 eV, C–O bonds at ∼286 eV, and O═C–O bonds at ∼288–289 eV,[65] revealing that the carbon framework remains unaffected following polysulfide interaction across all the electrodes. Ti 2p spectra (Fig. 5a) recorded before and after Li_2S_6 soaking show that all TiO_2-containing electrodes maintain a Ti $2p_{3/2}$ peak at 458.7 eV, characteristic of the Ti^{4+} oxidation state in TiO_2,[63,68] with the Ti $2p_{1/2}$ peak appearing at ∼464.6 eV, resulting in a spin–orbit splitting of approximately 5.5 eV. After immersion in Li_2S_6, a Ti 2p shift of roughly 0.4 eV toward higher binding energy is observed, indicating a decrease in electron density around the metal centre.[70–72] O 1s spectra (Fig. 5b) after soaking reveal significant changes in oxygen chemical states: TiO_2-CFP shows increased contributions from Ti–OH (∼531.5 eV) and adsorbates (∼533 eV) compared to Ti–O lattice oxygen (∼530 eV),[67–69] indicating polysulfide interaction with surface hydroxyl groups. Ni 2p spectra (Fig. 5c) after Li_2S_6 soaking show that NiO/TiO_2-CFP maintains its Ni^{2+} character with Ni $2p_{3/2}$ at ∼855 eV and characteristic satellite peaks at ∼862 eV typical of the NiO spectrum, while Ni/TiO_2 maintains its metallic Ni signature with Ni $2p_{3/2}$ at ∼852.7 eV.[40,56] The notably increased noise and broader peaks may indicate surface oxidation or the formation of Ni–S interactions that enhance polysulfide trapping without complete oxidation of the metallic nickel core, thereby demonstrating that both nickel oxidation states contribute to polysulfide immobilization through distinct chemical mechanisms.[70,73] S 2p spectra (Fig. S3c) of the composites after soaking in lithium polysulfide show that the signals at 167.8 and 168.6 eV are attributed to thiosulfate and polythionate complexes. The newly emerging peaks at 164 and 162 eV are attributed to bridging sulfur ($S_B^{\,0}$) and terminal sulfur ($S_T^{\,-1}$), respectively. The shuttle issue is mitigated by the polythionate species acting as mediators.[74] Furthermore, a significant chemical affinity between lithium polysulfides and nickel/titanium atoms is indicated by the development of S–Ti bonds (164.93 eV) and S–Ni bonds (162.08 eV).[74,75] Overall, XPS analysis indicates the successful modification of the materials and verifies the co-existence of the nickel and titanium oxidation states in the composites, as well as their interaction with Li_2S_6, indicating the adsorption of polysulfides and the role of nickel and titanium in counteracting the shuttle effect.

A comparative study of polysulfide adsorption characteristics of different TiO_2-based electrodes as cathodes and a lithium chip as the anode was conducted using a beaker cell test. Fig. S4a shows the gradual decolourisation of the polysulfide solution after the insertion of TiO_2-CFP for 3 h, 6 h and 12 h, respectively. This suggests that TiO_2-CFP exhibited the strongest adsorption ability among the three electrodes. Fig. S4b shows increased colour fading for NiO/TiO_2-CFP, reflecting good adsorption arising from surface modification. Fig. S4c also

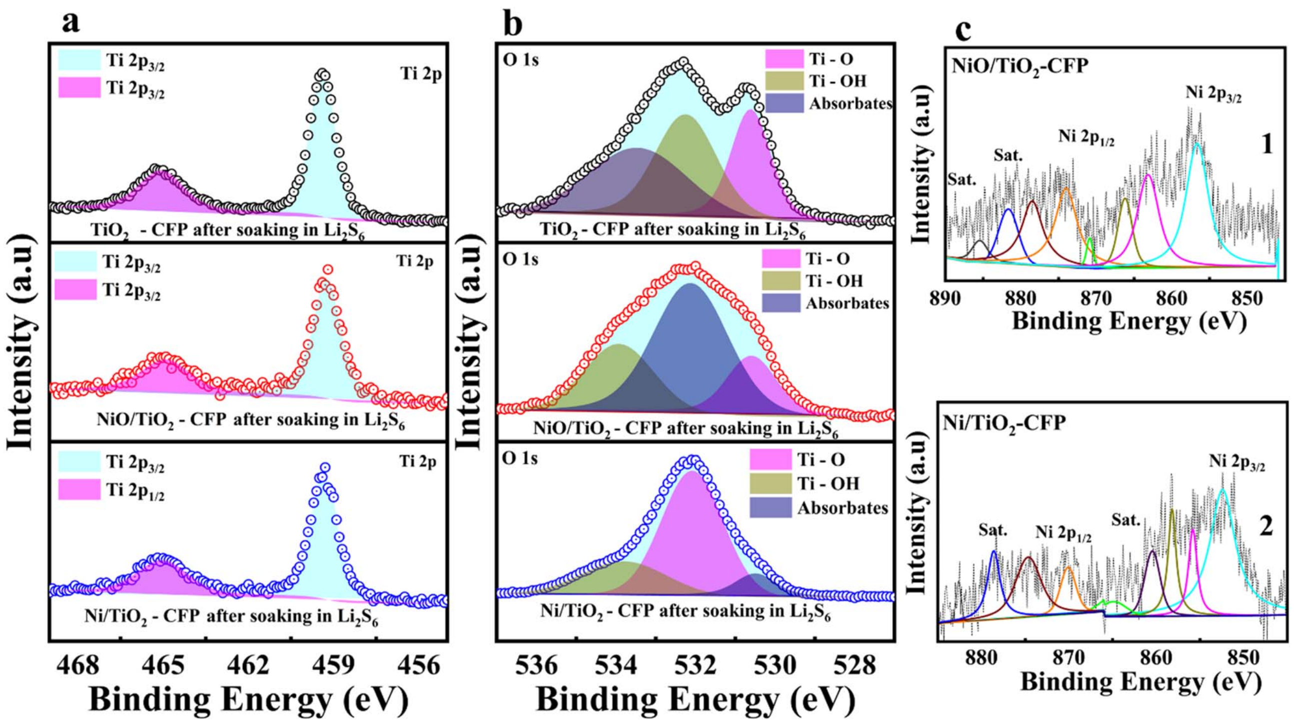

Fig. 5 XPS characterization of TiO_2-CFP, NiO/TiO_2-CFP, and Ni/TiO_2-CFP electrodes after soaking in Li_2S_6 solution: (a) Ti 2p, (b) O 1s, (c) Ni 2p (1) and Ni 2p (2).

indicates decolourisation for Ni/TiO_2-CFP, suggesting improved adsorption ability.

3.2 Effect on the kinetics of redox

The effect of TiO_2 nanotubes modified with NiO and Ni nanoparticles on the redox reaction kinetics in Li–S cells was investigated. Fig. 6 presents the cyclic voltammetry (CV) curves of cells with TiO_2-CFP, NiO/TiO_2-CFP, and Ni/TiO_2-CFP electrodes at 0.1 mV s^{-1}, respectively. The CV profiles of the three cells were compared to evaluate the catalytic influence of the TiO_2-based samples on the redox chemistry of sulfur species. Two pairs of reversible redox peaks were observed in the CV curves of all three TiO_2 based electrode cells. For each redox pair, the peaks were relatively sharp, suggesting faster kinetics and catalytic activity for the conversion of LiPSs.[76] The first pair of cathodic peaks found in the CV curve of the TiO_2 based electrode cells was assigned to the reduction of S_8 to Li_2S_4 (peak a) and the subsequent electrochemical reduction of Li_2S_4 to Li_2S (peak b). The corresponding anodic peaks were attributed to the electrochemical oxidation of Li_2S to Li_2S_4 (peak c) and the final oxidation of Li_2S_4 to S_8 (peak d), respectively.[77] The peak-to-peak separation (ΔE) between the anodic and cathodic peaks reflects the reversibility and the kinetic efficiency of the redox process.[78,79] Each pair of peaks (oxidation and reduction) shows similar redox conversion pathways during cycling, as shown in Fig. 6a–c. It is worth noting that their respective pair of peaks correspond to the chemical reactions associated with the electrochemical reduction from long-chain S_8 to Li_2S_4 and the electrochemical oxidation from Li_2S_4 to soluble high-order S_8, respectively.[77] However, their respective peak-to-peak separation varies due to chemical conversion rates. Therefore, peak-to-peak separation (ΔE) between pairs of peaks for cells with TiO_2-CFP, NiO/TiO_2-CFP and Ni/TiO_2-CFP electrodes are 0.24 V, 0.22 V and 0.20 V, respectively. These results indicated that the Ni/TiO_2-CFP electrode exhibited the lowest polarization and the fastest polysulfide conversion, while cells with the TiO_2-CFP and NiO/TiO_2-CFP electrodes showed relatively slower reaction kinetics and a slightly higher polarization.

Furthermore, CV profiles of all cells with TiO_2-based electrodes were recorded at various scan rates ranging from 0.1 to 0.5 mV s^{-1}, as shown in Fig. 7(a–c). The corresponding linear fittings of the peak currents *versus* the square root of the scan rates ($v^{1/2}$) for peak A, peak B, and peak C were obtained from the CV curves in (*a–c*) as presented in Fig. 7(d–g). However, the purpose of the linear fittings was to determine the slopes used to calculate lithium-ion diffusion in the respective cathode materials. According to the Randles–Sevcik equation, there is a linear relationship between the redox peak current and the square root of the scan rate, which makes it possible to evaluate the diffusion of lithium ions within the electrodes:[80]

$$I_\mathrm{p} = 2.69 \times 10^5 \times n^{3/2} \times A \times {D_{\mathrm{Li}^+}}^{1/2} \times C_{\mathrm{Li}^+} \times v^{1/2};$$

where D_{Li^+} is the Li^+ diffusion coefficient (cm^2 s^{-1}), C_{Li^+} is the concentration of lithium ions in the electrolyte (mol cm^{-3}), v is the scan rate (V s^{-1}), I_p is the peak current (A), n is the number of electrons, and A is the electrode area (1.13097 cm^2).

$${D_{\mathrm{Li}^+}}^{1/2} = \frac{1}{(2.69 \times 10^5) \times n^{3/2} \times A \times C_{\mathrm{Li}^+}} \times \frac{i_\mathrm{p}}{v^{1/2}};$$

While the electrode area, the number of electrons (assumed to be 2 electrons), and the concentration of lithium ions in the electrolyte remained constant, the diffusion coefficient D_{Li^+} was determined from the slope of the curve ($I_\mathrm{p}/v^{0.5}$), which reflected the diffusion rate of lithium ions, as shown in Table 1.[74] It was evident that the cell with the Ni/TiO_2-CFP electrode exhibited the highest lithium-ion diffusivity at peaks A and D, which mainly arose from improved lithium polysulfide adsorption and enhanced conversion of LiPSs to Li_2S. Diffusion coefficients (D) were deduced according to the Randles–Sevcik equation based on a 12 mm electrode surface and a 1 M polysulfide solution. From Table 1, peak A, corresponding to the fastest redox process, showed that the cell with the Ni/TiO_2-CFP electrode exhibited the highest value of D (5.75×10^{-6} cm^2 s^{-1}), indicating rapid ion transport and effective electrochemical conversion. By contrast, peak C exhibited intermediate diffusion behaviour with a value of 2.91×10^{-6} cm^2 s^{-1} for Ni/TiO_2, suggesting a moderately rapid electrochemical process. For all peaks, the cell with the Ni/TiO_2 electrode exhibited the highest diffusion coefficients, followed by cells with NiO/TiO_2-CFP and

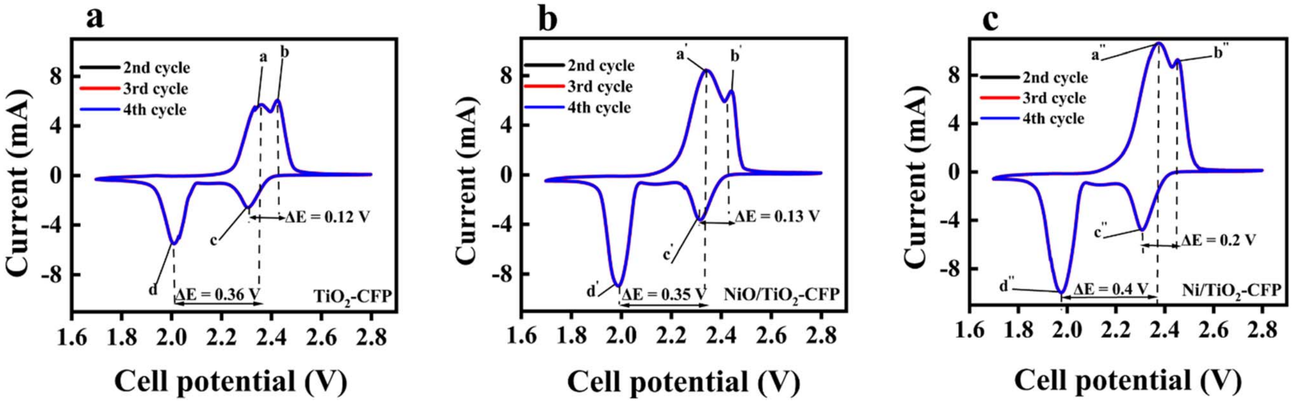

Fig. 6 Comparative cyclic voltammetry (CV) curves at 0.1 mV s^{-1} for all electrodes: (a) TiO_2-CFP, (b) NiO/TiO_2-CFP and (c) Ni/TiO_2-CFP.

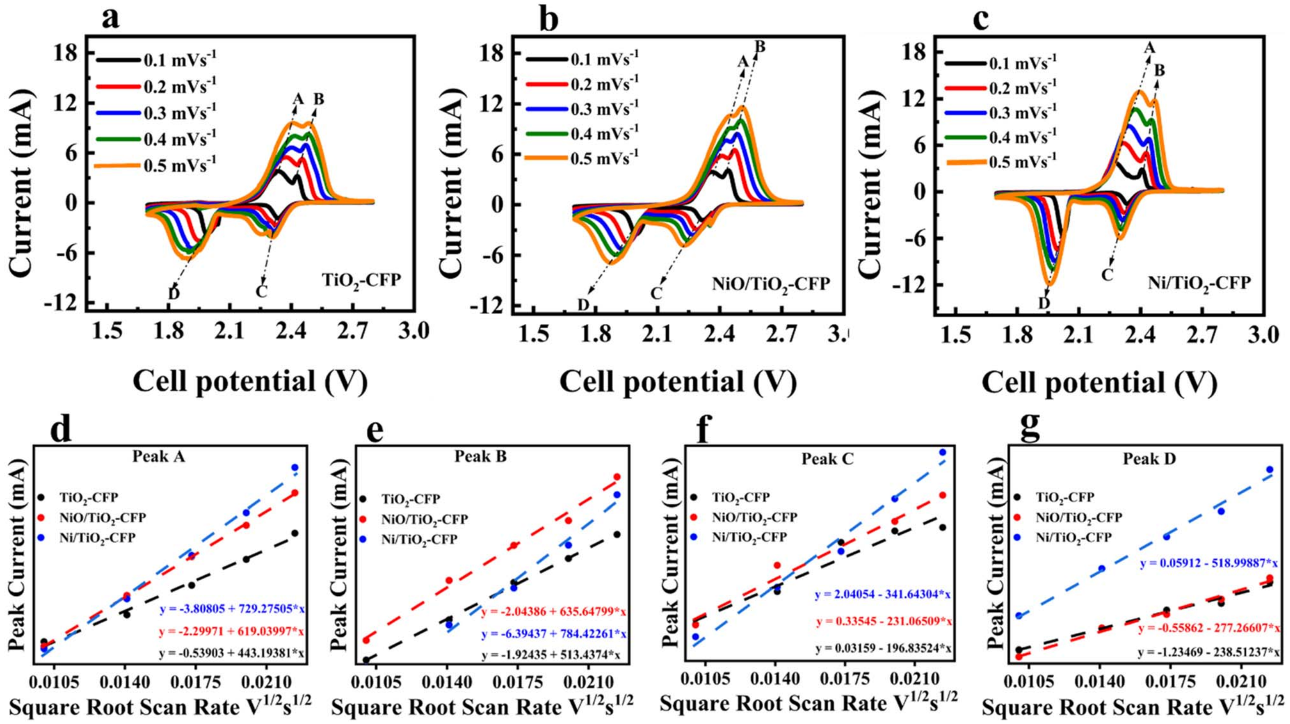

Fig. 7 CV profiles of electrodes recorded at various scan rates ranging from 0.1 to 0.5 mV s^{-1}: (a) TiO$_2$-CFP, (b) NiO/TiO$_2$-CFP, (c) Ni/TiO$_2$-CFP and (d–g) the linear fittings of the peak currents *versus* the square root of the scan rates ($\nu^{1/2}$).

Table 1 Li$^+$ diffusion coefficient (D_{Li^+}) values of TiO$_2$, NiO/TiO$_2$ and Ni/TiO$_2$

Electrodes	Peak A	Peak B	Peak C	Peak D
TiO$_2$-CFP	2.12×10^{-6}	3.56×10^{-7}	4.19×10^{-7}	6.15×10^{-7}
NiO/TiO$_2$-CFP	4.14×10^{-6}	5.46×10^{-7}	5.77×10^{-7}	8.31×10^{-7}
Ni/TiO$_2$-CFP	5.75×10^{-6}	8.31×10^{-7}	1.26×10^{-6}	2.91×10^{-4}

TiO$_2$-CFP electrodes. Therefore, the cell with the Ni/TiO$_2$-CFP electrode showed better electrochemical kinetics for all redox peaks, indicating that this material is a promising electrode for improved rate performance in lithium–sulfur batteries. Generally, the best diffusion enhancement for cells with the Ni/TiO$_2$-CFP electrode can be attributed mainly to the presence of the metallic Ni phase, which provides better electronic conductivity, promotes the transport of Li$^+$ and polysulfides, and facilitates rapid interfacial charge transfer. Moreover, this phenomenon suggests faster liquid–liquid conversion of LiPSs on the electrode surface.[81]

Cyclic voltammetry obtained from symmetric cells (Fig. 8) illustrates the conversion of lithium polysulfides. It can be observed from Fig. S5 that the TiO$_2$-CFP electrode's cyclic voltammetry for all scan rates exhibited very broad, weak peaks, indicating high resistance and sluggish reaction kinetics. In Fig. 8a, cells with Ni/TiO$_2$-CFP and NiO/TiO$_2$-CFP electrodes at a scan rate of 1 mV s^{-1} showed moderate resistance, whereas the TiO$_2$-CFP electrode exhibited broad loops, indicating high resistance. Moreover, cells with Ni/TiO$_2$-CFP and NiO/TiO$_2$-CFP electrodes at a scan rate of 10 mV s^{-1}, as shown in Fig. 8b, showed more symmetric peaks and improved kinetics, while the thinner, more symmetric loops reflected lower polarization.[82,83] Cells with Ni/TiO$_2$-CFP and NiO/TiO$_2$-CFP electrodes at a scan rate of 20 mV s^{-1} as shown in Fig. 8c displayed symmetric peaks, suggesting excellent reversibility and low resistance, as evidenced by thin and overlapping curves. With increasing scan rates, cells with Ni/TiO$_2$-CFP and NiO/TiO$_2$-CFP electrodes generally exhibited better kinetic performance and lower resistance, according to the symmetric cell results. The 20 mV s^{-1} scan rate gave the most pronounced symmetric peaks and the best reversibility.

The potentiostatic charge–discharge behaviour of cells with TiO$_2$-based electrodes was evaluated using the Li$_2$S nucleation test. The cell with TiO$_2$-CFP reached the highest current at a time of ~8370 s, as shown in Fig. 9a. This value is the highest when compared with the peak response time (~7211 s) of the cell with the NiO/TiO$_2$-CFP electrode (Fig. 9b) and the peak response time (~5970 s) of the cell with the Ni/TiO$_2$-CFP electrode (Fig. 9c), respectively. It is worth noting that the cell with Ni/TiO$_2$-CFP exhibited the best performance, because it reached the highest current after approximately 5970 s, suggesting accelerated Li$_2$S growth.[56] The maximum Li$_2$S deposition capacity was also determined for all TiO$_2$-based cells. The calculated Li$_2$S nucleation capacities of all TiO$_2$-based cells were 465 mA h g^{-1}, 600 mA h g^{-1} and 746 mA h g^{-1} for TiO$_2$-CFP, NiO/TiO$_2$-CFP and Ni/TiO$_2$-CFP electrodes, respectively. The cell with the Ni/TiO$_2$-CFP electrode exhibited the highest value and therefore showed excellent catalytic activity toward LiPSs,

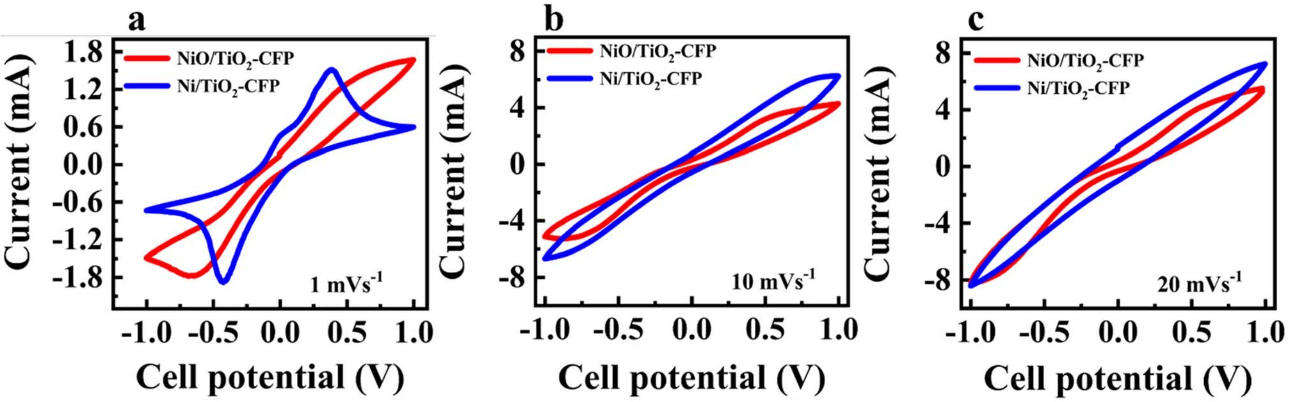

Fig. 8 CV curves of Li_2S_6 symmetric cells with NiO/TiO_2 and Ni/TiO_2 based electrodes at varying scan rates: (a) 1 mV s^{-1}, (b) 10 mV s^{-1} and (c) 20 mV s^{-1}.

thereby accelerating Li_2S redox kinetics during the electrochemical process.

The charge transfer resistance (R_{ct}) and the diffusion process associated with the Warburg impedance (Z_w) are shown by a semicircle in the high-frequency region and a sloping line in the low-frequency region of the Nyquist plots (Fig. 10). It is evident that the charge transfer resistance (R_{ct}) of cells with TiO_2-CFP, NiO/TiO_2-CFP and Ni/TiO_2-CFP electrodes decreased with decreasing semicircle diameter, indicating lower kinetic impedance. The charge transfer resistance values obtained for the respective cells with TiO_2 based electrodes were 46 Ω, 32 Ω and 14 Ω, respectively. The cell with the Ni/TiO_2-CFP electrode showed the smallest initial resistance ($R_{ct} \approx 14$ Ω), reflecting enhanced kinetic activity, whereas cells with NiO/TiO_2-CFP ($R_{ct} \approx 32$ Ω) and TiO_2-CFP ($R_{ct} \approx 46$ Ω) electrodes showed higher R_{ct} values primarily owing to less efficient electron transport pathways. This kinetic facilitation is important because lower R_{ct} values reflect faster charge transport as well as accelerated redox reaction functions.[84]

3.3 Cycling performance of modified TiO_2-based cathodes

The charge–discharge cycling characteristics of Li–S cells with TiO_2-based electrodes, namely, TiO_2-CFP, NiO/TiO_2-CFP, and Ni/TiO_2-CFP, at a sulfur loading of 2 mg cm^{-2} were assessed as shown in Fig. 11a. At 0.5C, these cells exhibited promising initial capacities of 1053, 912, and 845 mA h g^{-1}, respectively. After 100 cycles, the cell with the TiO_2-CFP electrode showed the highest capacity retention of approximately 97%. In contrast, the retention for cells with NiO/TiO_2-CFP and Ni/TiO_2-CFP electrodes decreased to approximately 70% and 74%, respectively. The coulombic efficiencies (CEs) were approximately 90%, 91%, and 87%, respectively, for each cell. In cells with a TiO_2-CFP electrode, the capacity decreased steadily, with a sudden drop in capacity during initial cycles, after which relatively stable performance was observed. Nevertheless, this is expected to be due to the inefficiency of TiO_2 in holding the sulfur species, mainly due to the low conductivity of the material, which affects the electrochemical reactions. This behaviour is characteristic of TiO_2-based hosts, which have limited conductivity. As a result, the electrochemical cycling performance declines over time, leading to a gradual loss of capacity.[85,86] Similar to the cell with NiO/TiO_2-CFP, the capacity fading is evident in the first 15 cycles. However, it continues to decline steadily to 600 mA h g^{-1} due to the lack of sufficient conductivity for long-term cycling.[87] In contrast, after Ni/TiO_2-CFP's initial discharge, the capacity remains relatively stable, showing minimal decline in the first 50 cycles. By the 100th cycle, the capacity remains around 730 mA h g^{-1}, confirming

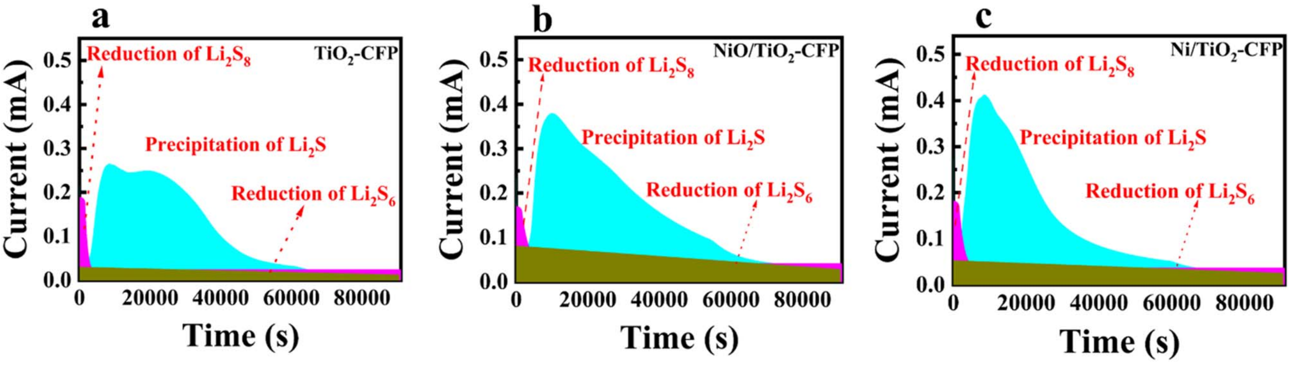

Fig. 9 Potentiostatic discharge of cells with (a) TiO_2-CFP, (b) NiO/TiO_2-CFP and (c) Ni/TiO_2-CFP.

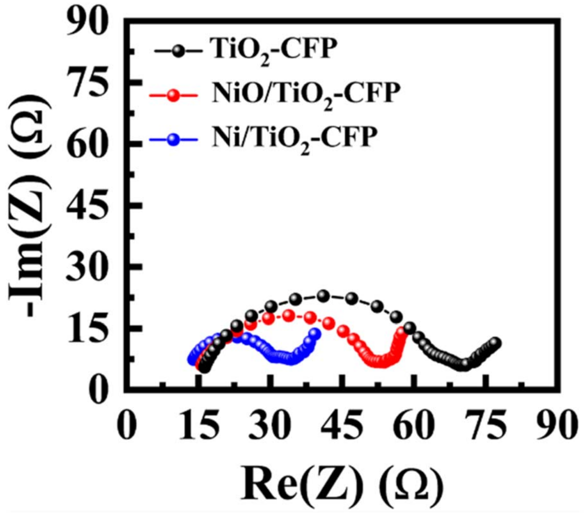

Fig. 10 Electrochemical impedance spectroscopy profiles for cells with TiO_2-based electrodes.

that the Ni-modified electrode has the best capacity retention among the three configurations. Adding the metal Ni enhances the conductivity of the material and provides more active catalytic sites for the conversion of lithium polysulfides. This enhances electrochemical reactions, keeping the sulfur species under control.[53,88] It is also worth noting that the specific capacity achieved for this rate and mass loading was higher than those of previously reported TiO_2-based electrodes.[89,90] The cycle stability with different cathode materials was investigated at 0.2C rates, as shown in Fig. 11b. Cells with TiO_2-CFP, NiO/TiO_2-CFP and Ni/TiO_2-CFP electrodes with areal sulfur mass loadings of 2 mg cm^{-2} exhibited initial discharge capacities of 1192, 1121 and 895 mA h g^{-1}, respectively. After 100 cycles, the cell with the Ni/TiO_2-CFP electrode retained 92% of its initial capacity. In contrast, the cells with NiO/TiO_2-CFP and TiO_2-CFP electrodes retained only 67% and 55%, respectively. In cells with TiO_2-CFP, it can be observed that during the first 5 cycles, the capacity decreases sharply to about 600 mA h g^{-1}. After that, capacity further decreases steadily, reaching about 500 mA h g^{-1} after the 100th cycle. This capacity trend is consistent with a TiO_2-based host, which provides polar adsorption sites for lithium polysulfides but has limited charge transport and reuse of dissolved intermediates. As the cycles progress, the active sulfur becomes less accessible. This is due to the well-known problem of lithium polysulfides, which dissolve and migrate during cycles, leading to a steady

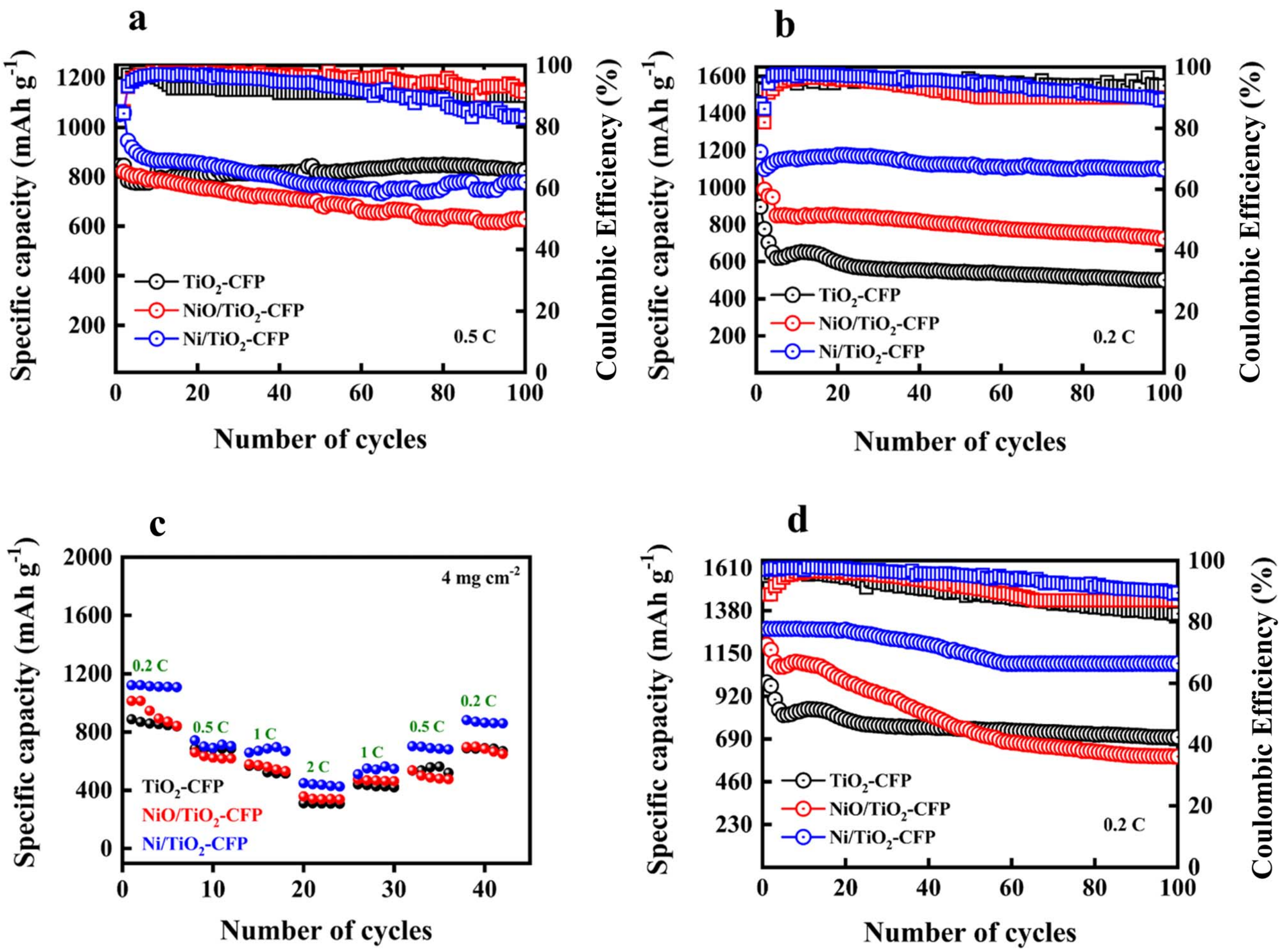

Fig. 11 Charge–discharge of cells with TiO_2-CFP, NiO/TiO_2-CFP and Ni/TiO_2-CFP electrodes: (a and b) cycling performance at 0.5C and 0.2C, respectively, (c) rate capability test and (d) cycling performance (4 mg cm^{-2}) at 0.2C.

reduction of sulfur utilization and capacity fade.[91,92] For NiO/TiO_2-CFP, cycle 1 starts at a level above that of TiO_2-CFP, at 1121 mA h g^{-1}, and then it decreases gradually as the cycles progress, reaching a plateau at a level of 830–850 mA h g^{-1}. Thereafter, the capacity continues to slowly decrease with increasing cycles, reaching 720 to 750 mA h g^{-1} at cycle 100. The presence of NiO creates polarity and chemical interaction that more effectively captures lithium polysulfides compared to TiO_2-CFP. However, the NiO material is not a highly conductive metallic phase, and the electrode does not fully eliminate slow kinetic limitations and gradual loss of accessible sulfur over many cycles.[93] However, Ni/TiO_2-CFP's first cycle begins at 1192 mA h g^{-1}. For the first few cycles, the capacity increases slightly before remaining nearly flat with a gradual capacity loss, still close to 1100 mA h g^{-1} after 100 cycles. This is consistent with the presence of metallic Ni that enables better electronic conductivity and accelerates the rate of polysulfide conversion reactions to ensure that the sulfur redox reactions remain reversible and that more active material is electrochemically accessible after cycling.[94,95] This demonstrates that the cell with the Ni/TiO_2 electrode is most effective at trapping and reactivating LiPSs compared to other TiO_2-based electrodes reported in the literature.[53,54,89] Furthermore, the rate capability test of cells with TiO_2-CFP, NiO/TiO_2-CFP, and Ni/TiO_2-CFP electrodes was performed as illustrated in Fig. 11c. At current densities of 0.2, 0.5, 1, and 2C, the cells initially generated capacities of approximately 1122, 1013.61, and 887.65 mA h g^{-1}, respectively, at 0.2C. When the current density was reverted to 0.2C, their respective capacities recovered to 787.58, 700 and 670 mA h g^{-1}. This indicates that while some irreversible capacity loss occurred, the TiO_2-based host significantly aids cell performance by mitigating LiPS shuttling and accelerating the redox kinetics of sulfur and its discharge products. Moreover, the cycling performance of all three cells with TiO_2 based electrodes was evaluated at a high sulfur mass loading of 4.0 mg cm^{-2} and a rate of 0.2C, as shown in Fig. 11d. The cell with the Ni/TiO_2-CFP electrode demonstrated superior performance with an initial specific capacity of approximately 1285 mA h g^{-1} at 0.2C with a decay rate of only 0.1%, while reaching 85% of the theoretical capacity (1C = 1675 mA h g^{-1}). After 100 cycles, the cell maintained a capacity of approximately 1095 mA h g^{-1}, demonstrating excellent capacity retention. In contrast, the cells with the NiO/TiO_2-CFP and TiO_2-CFP electrodes exhibited comparatively lower initial specific capacities of approximately 1196.4 and 995.72 mA h g^{-1}, respectively. Cells with the TiO_2-CFP electrode show relatively good capacity retention in the initial cycles, but the capacity quickly stabilizes to a low value of approximately 700 mA h g^{-1} by the 20th cycle. In contrast, cells with NiO/TiO_2-CFP electrodes demonstrated a rapid and significant capacity fade over the first 40–60 cycles. The capacity drops steadily to roughly 550 mA h g^{-1} by the end of 100 cycles, indicating structural instability or poor suppression of the polysulfide shuttle effect.[87,92] The coulombic efficiencies of cells with TiO_2-CFP, NiO/TiO_2-CFP and Ni/TiO_2-CFP electrodes were determined to be 96%, 90% and 86% respectively. The superior specific capacity of the cell with the Ni/TiO_2-CFP electrode compared to the other electrodes can be attributed to its enhanced electrical conductivity and effective electron transport pathways, which accelerated the conversion of polysulfides into Li_2S.[53,93,94]

Notably, cells with the Ni/TiO_2-CFP electrode outperformed those with other TiO_2-CFP electrodes with higher sulfur loadings with low current rates.[39,54] In summary, comprehensive electrochemical analysis reveals that the cells with the Ni/TiO_2-CFP electrode significantly outperform their TiO_2-CFP and NiO/TiO_2-CFP electrode counterparts in terms of capacity retention, reaction rate and cycling stability, particularly under challenging conditions of high sulfur loading (4.0 mg cm^{-2}).

The galvanostatic charge–discharge profiles of Li–S cells within the voltage window of 1.6–2.8 V *vs.* Li^+/Li at a current rate of 0.2C were assessed, as illustrated in Fig. 12. Every voltage profile shows a single charge plateau at about 2.4 V and two separate discharge plateaus at roughly 2.3 V and 2.1 V. These characteristics align with the typical redox reactions of sulfur species. In particular, the discharge plateaus show how elemental sulfur (S_8) is gradually reduced to long-chain LiPSs and then further reduced to short-chain LiPSs (Li_2S_2/Li_2S).[96–98] The reverse oxidation of LiPSs to elemental sulfur is reflected in the charge plateau at about 2.4 V. As indicated in Fig. 12a, the cell with the TiO_2-CFP electrode had the lowest specific capacity of 1091 mA h g^{-1}. In contrast, cells with NiO/TiO_2-CFP and Ni/TiO_2-CFP electrodes produced capacities of 1170 mA h g^{-1} and 1283 mA h g^{-1} at the 5th cycle. Moreover, cells with the Ni/TiO_2 electrode showed the lowest voltage hysteresis ($\Delta E = 0.25$ V) compared with cells with NiO/TiO_2-CFP and TiO_2-CFP electrodes, indicating improved charge transfer. The galvanostatic charge–discharge profiles of the cells with the Ni/TiO_2-CFP electrode at different cycles were also assessed, as shown in Fig. 12b. This figure illustrates how cells with the Ni/TiO_2-CFP electrode performed when cycled under galvanostatic discharge and charge cycles, from the 2nd to the 100th cycle at 0.2C. Initially, the voltage plateau remains stable; however, from cycle number 50, there is already a noticeable gradual loss of capacity and an increase in the polarization gap (ΔE), which may be regarded as the onset of degradation. Subsequently, with increasing cycles, capacity loss becomes prominent, and discharge voltage moves lower, indicating irreversible loss and continued degradation. The increase in the polarization gap and reduction in plateau regions indicate that, with extensive cycling, structural changes in the modified material and an increase in irreversible resistance compromise its stability and electrochemical performance.

To further evaluate the structural integrity of the Ni/TiO_2 electrode after cycling, post-cycling SEM analysis was performed, and the results are presented in Fig. S6. The low-magnification SEM image (Fig. S6a) confirms that the carbon fibre strand retains its structural stability, with the Ni/TiO_2 nanostructure coating remaining conformally adhered to the fibre surface after repeated charge–discharge cycling. At a similar magnification in Fig. S6b, the cycled electrode surface displays interconnected sheet-like and globular features, consistent with the deposition of Li_2S discharge products and residual active material, indicative of active polysulfide conversion during cycling. The high-magnification image

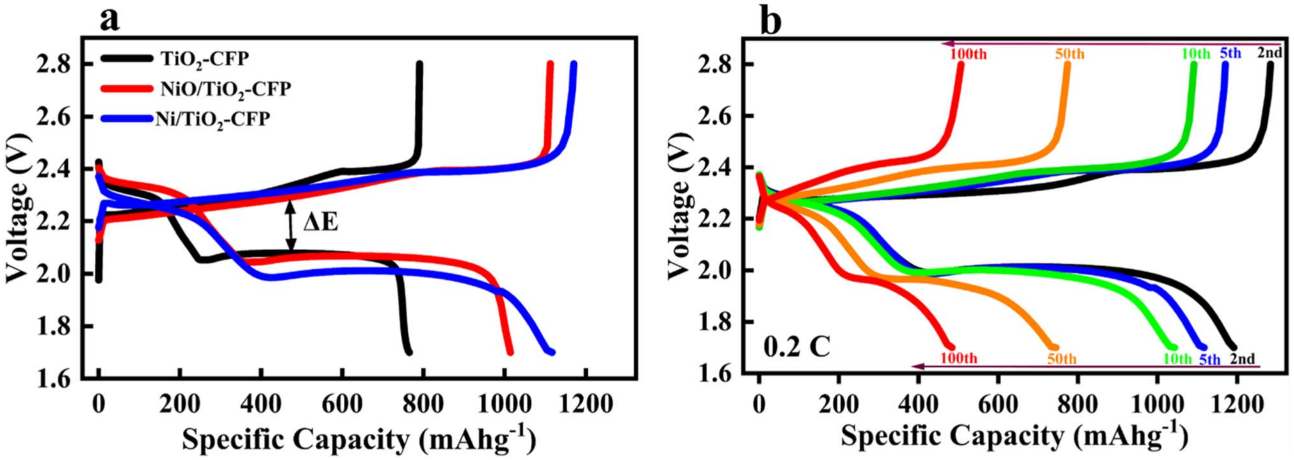

Fig. 12 Galvanostatic charge–discharge profiles of cells with TiO_2-CFP, NiO/TiO_2-CFP and Ni/TiO_2-CFP electrodes (a) at the 5th cycle and (b) Ni/TiO_2-CFP electrodes at the 2nd, 5th, 10th, 50th and 100th cycles, respectively.

(Fig. S6c) further reveals that the nanostructured surface morphology of the Ni/TiO_2 composite is largely preserved, with no evidence of structural collapse, consistent with the low-capacity decay rate per cycle observed electrochemically. EDS elemental mapping confirms the uniform spatial distribution of sulfur (S), titanium (Ti), and nickel (Ni) across the post-cycled

Table 2 Comparison of the electrochemical performance of TiO_2-based nanotubes

Cathode additive	Average particle size (nm)	Discharge capacity (mA h g^{-1})	Long-term cycling performance	C-rate (C)	Sulfur loading (mg cm^{-2})	Paper/study
Ni/TiO_2 nanotubes	∼18.3	1053	100	0.5	2.0	This work
		1192	100	0.2	2.0	
		1285	100	0.2	4.0	
NiO/TiO_2 nanotubes		912	100	0.5	2.0	
		1121	100	0.2	2.0	
		1136	100	0.2	4.0	
TiO_2 nanotubes		845	100	0.5	2.0	
		895	100	0.2	2.0	
		995	100	0.2	4.0	
TiO_2-supported Nb catalyst		575	350	3.0	1.0	54
		777	100	0.1	5.0	
		966	100	0.2	1.0	
TiO_2-based nanotube	10.2	721	100	0.2	1.0	
		484	350	3.0	1.0	
		632	100	0.1	5.0	
TiO_2-Ru@S	3–4.5	827	200	0.5	Not reported	53
		710	700	2.0	Not reported	
		1085	140	0.1	3.0	
TiO_2@S		1264	30	0.02	4.8	
		471	200	0.5	Not reported	
S@WS_2–TiO_2		560.9	1100	1	1.1	39
		455.1	100	0.2	5.878	
S@MoS_2–TiO_2		634	1100	1	1.1	
		503.8	100	0.2	5.867	
S@TiO_2		422.76	1100	1	1.1	
TiO_2(B)-NTs	7	1055	50	0.1	1.5–2.0	89
		805	80	1.0	1.5–2.0	
		235	600	5.0	1.5–2.0	
S-TNT@CNT		837	200	0.5	1.2–1.8	
		510	80	1.0	1.2–1.8	
TiO_2/S 1 : 1	80–100	795	100	0.2	1.1	99
TiO_2/S 1 : 2	∼110	913	100	0.2	1.1	
TiO_2 NTs-S	∼300	852	100	0.1	1.6	40
TiO_2 NTs@Ni–S		1163	100	0.1	1.6	
HGN@TiO_2@C/S		626.8	200	1	Not reported	71

surface (Fig. S6d), demonstrating effective polysulfide retention within the cathode and homogeneous dispersion of the Ni/TiO_2 active species. These observations collectively confirm the structural and chemical stability of the Ni/TiO_2-CFP electrode, providing direct morphological evidence for its superior long-term electrochemical performance.

As shown in Table 2, a detailed comparison of TiO_2 based nanotubes with varying average particle sizes and sulfur mass loadings is presented with their respective electrochemical performance in terms of specific capacities and cycling stability.

4 Conclusion

In summary, this work presents the development and systematic electrochemical evaluation of anatase TiO_2 nanotubes (an average diameter of approximately 18.3 nm) synthesized *via* hydrothermal treatment. These nanotubes were decorated with Ni nanoparticles through hydrogen-assisted reduction, at a 10 : 1 molar ratio. ICP-OES analysis confirmed the molar ratio of bifunctional additives. These heterostructures were subsequently incorporated into carbon fibre paper (CFP) to form TiO_2-CFP, NiO/TiO_2-CFP and Ni/TiO_2-CFP composite cathodes, evaluated at a sulfur loading of 4 mg cm^{-2}. The use of these modified heterostructures significantly improved the electrochemical characteristics compared to the cell with bare TiO_2-CFP, as confirmed by galvanostatic charge–discharge tests, cyclic voltammetry (CV), and electrochemical impedance spectroscopy (EIS). The cell with Ni/TiO_2-CFP exhibited the best overall performance, delivering an initial specific capacity of 1285 mA h g^{-1} at 0.2C with a capacity decay rate of only 0.1% per cycle, retaining approximately 1095 mA h g^{-1} after 100 cycles at a coulombic efficiency of 96%. Even at higher current rates (2C), Ni/TiO_2-CFP (381.52 mA h g^{-1}) demonstrated superior rate capability, outperforming both cells with NiO/TiO_2-CFP (301.14 mA h g^{-1}) and TiO_2-CFP (230.27 mA h g^{-1}), respectively. The charge–discharge profiles of the cell with Ni/TiO_2-CFP showed minimal polarization, confirming stable lithium polysulfide retention and efficient electrocatalytic conversion. EIS measurements confirmed the lowest charge transfer resistance (14 Ω) for Ni/TiO_2, alongside the highest Li_2S nucleation capacity (746 mA h g^{-1}), collectively indicating significantly faster interfacial kinetics and superior ion transport. The NiO/TiO_2-CFP cell demonstrated intermediate characteristics, with an initial specific capacity of 1196.4 mA h g^{-1} at 0.2C, attributed to enhanced polysulfide chemisorption through abundant Ni^{2+}/Ni^{3+} redox active sites and improved chemisorption, but limited by lower long-term conductivity relative to metallic Ni. Meanwhile, the cell with TiO_2-CFP demonstrated the weakest performance, delivering an initial specific capacity of 995.72 mA h g^{-1} at 0.2C, constrained by its intrinsically low electronic conductivity and weak electrocatalytic activity, despite enabling moderate polysulfide adsorption through its polar surface sites. Overall, the synergistic interaction of the conductive Ni nanoparticles and the stable, high surface area TiO_2 nanotube host resulted in improved electrocatalytic activity, enhanced charge transport, and superior interfacial stability, establishing Ni/TiO_2-CFP as a rational and scalable cathode architecture for high sulfur loading lithium–sulfur batteries. Future work could extend this strategy by systematically varying Ni loading and by evaluating the architecture under pouch cell conditions.

Author contributions

Emmanuel Siaw: writing – original draft, validation, methodology, investigation, and data curation. Dias Bekeshov: methodology and investigation. Alas Alaskhanov: methodology and investigation. Aishuak Konarov: methodology and validation. Zhumabay Bakenov: validation and supervision. Nurzhan Baikalov: writing – review & editing, supervision, methodology, investigation, and funding acquisition. Stavros Poulopoulos: writing – review & editing, validation, supervision, and funding acquisition.

Conflicts of interest

The authors declare that they have no known competing financial interests or personal relationships that could have appeared to influence the work reported in this paper.

Data availability

The authors confirm that any data that support the findings of this study are included within the article and included as a part of the supplementary information (SI). Upon reasonable request, raw data regarding this work can be requested from the corresponding author.

Supplementary information is available. See DOI: https://doi.org/10.1039/d6na00263c.

Acknowledgements

This work was funded by the Science Committee of the Ministry of Science and Higher Education of the Republic of Kazakhstan (grant No. AP23490764).

References

1 W. Qian, Y. Guo, W. Zuo, X. Wu and L. Zhang, Toward Practical Lithium–Sulfur Batteries, *Mater. Chem. Front.*, 2024, **8**(14), 2556–2577, DOI: 10.1039/D4QM00180J.

2 D. Deng, Li-ion Batteries: Basics, Progress, and Challenges, *Energy Sci. Eng.*, 2015, **3**(5), 385–418, DOI: 10.1002/ese3.95.

3 M. Fichtner, Recent Research and Progress in Batteries for Electric Vehicles, *Batteries Supercaps*, 2022, **5**(2), e202100224, DOI: 10.1002/batt.202100224.

4 B. Song, L. Su, X. Liu, W. Gao, T. Wang, Y. Ma, Y. Zhong, X. Cheng, Z. Zhu, J. He and Y. Wu, An Examination and Prospect of Stabilizing Li Metal Anode in Lithium–Sulfur Batteries: A Review of Latest Progress, *Electron*, 2023, **1**(2), e13, DOI: 10.1002/elt2.13.

5 K. R. Ngoy, V. T. Lukong, K. O. Yoro, J. B. Makambo, N. C. Chukwuati, C. Ibegbulam, O. Eterigho-Ikelegbe, K. Ukoba and T.-C. Jen, Lithium-Ion Batteries and the

Future of Sustainable Energy: A Comprehensive Review, *Renewable Sustainable Energy Rev.*, 2025, **223**, 115971, DOI: 10.1016/j.rser.2025.115971.

6 N. Baikalov, R. Agassultanov, Z. Sagyngerey, S. Sariyev, A. Tokenov, Z. Bakenov and A. Konarov, High Voltage LiMn$_x$Fe$_{1-x}$PO$_4$@NC Cathode Material for Lithium-Ion Rechargeable Batteries, *J. Electroanal. Chem.*, 2026, **1001**, 119670, DOI: 10.1016/j.jelechem.2025.119670.

7 S. G. Booth, A. J. Nedoma, N. N. Anthonisamy, P. J. Baker, R. Boston, H. Bronstein, S. J. Clarke, E. J. Cussen, V. Daramalla, M. De Volder, S. E. Dutton, V. Falkowski, N. A. Fleck, H. S. Geddes, N. Gollapally, A. L. Goodwin, J. M. Griffin, A. R. Haworth, M. A. Hayward, S. Hull, B. J. Inkson, B. J. Johnston, Z. Lu, J. L. MacManus-Driscoll, X. Martínez De Irujo Labalde, I. McClelland, K. McCombie, B. Murdock, D. Nayak, S. Park, G. E. Pérez, C. J. Pickard, L. F. J. Piper, H. Y. Playford, S. Price, D. O. Scanlon, J. C. Stallard, N. Tapia-Ruiz, A. R. West, L. Wheatcroft, M. Wilson, L. Zhang, X. Zhi, B. Zhu and S. A. Cussen, Perspectives for next Generation Lithium-Ion Battery Cathode Materials, *APL Mater.*, 2021, **9**(10), 109201, DOI: 10.1063/5.0051092.

8 H. Niu, N. Zhang, Y. Lu, Z. Zhang, M. Li, J. Liu, N. Zhang, W. Song, Y. Zhao and Z. Miao, Strategies toward the Development of High-Energy-Density Lithium Batteries, *J. Energy Storage*, 2024, **88**, 111666, DOI: 10.1016/j.est.2024.111666.

9 H. Peng, T. Hou, Q. Zhang, J. Huang, X. Cheng, M. Guo, Z. Yuan, L. He and F. Wei, Strongly Coupled Interfaces between a Heterogeneous Carbon Host and a Sulfur-Containing Guest for Highly Stable Lithium-Sulfur Batteries: Mechanistic Insight into Capacity Degradation, *Adv. Mater. Interfaces*, 2014, **1**(7), 1400227, DOI: 10.1002/admi.201400227.

10 W. Kou, X. Li, Y. Liu, X. Zhang, S. Yang, X. Jiang, G. He, Y. Dai, W. Zheng and G. Yu, Triple-Layered Carbon-SiO$_2$ Composite Membrane for High Energy Density and Long Cycling Li–S Batteries, *ACS Nano*, 2019, **13**(5), 5900–5909, DOI: 10.1021/acsnano.9b01703.

11 W. Chen, T. Qian, J. Xiong, N. Xu, X. Liu, J. Liu, J. Zhou, X. Shen, T. Yang, Y. Chen and C. Yan, A New Type of Multifunctional Polar Binder: Toward Practical Application of High Energy Lithium Sulfur Batteries, *Adv. Mater.*, 2017, **29**(12), 1605160, DOI: 10.1002/adma.201605160.

12 Z. Guo, H. Nie, Z. Yang, W. Hua, C. Ruan, D. Chan, M. Ge, X. Chen and S. Huang, 3D CNTs/Graphene-S-Al$_3$ Ni$_2$ Cathodes for High-Sulfur-Loading and Long-Life Lithium–Sulfur Batteries, *Adv. Sci.*, 2018, **5**(7), 1800026, DOI: 10.1002/advs.201800026.

13 D. Liu, C. Zhang, G. Zhou, W. Lv, G. Ling, L. Zhi and Q. Yang, Catalytic Effects in Lithium–Sulfur Batteries: Promoted Sulfur Transformation and Reduced Shuttle Effect, *Adv. Sci.*, 2018, **5**(1), 1700270, DOI: 10.1002/advs.201700270.

14 M. R. Busche, P. Adelhelm, H. Sommer, H. Schneider, K. Leitner and J. Janek, Systematical Electrochemical Study on the Parasitic Shuttle-Effect in Lithium-Sulfur-Cells at Different Temperatures and Different Rates, *J. Power Sources*, 2014, **259**, 289–299, DOI: 10.1016/j.jpowsour.2014.02.075.

15 M. He, Y. Li, M. Safari and Q. Pang, Towards Practical High Energy Density Lithium-Sulfur Batteries, *CCS Chem.*, 2025, **7**(11), 3235–3258, DOI: 10.31635/ccschem.025.202506213.

16 Y. Fei and G. Li, Unveiling the Pivotal Parameters for Advancing High Energy Density in Lithium-Sulfur Batteries: A Comprehensive Review, *Adv. Funct. Mater.*, 2024, **34**(21), 2312550, DOI: 10.1002/adfm.202312550.

17 Y. Zhai, Y. Dou, D. Zhao, P. F. Fulvio, R. T. Mayes and S. Dai, Carbon Materials for Chemical Capacitive Energy Storage, *Adv. Mater.*, 2011, **23**(42), 4828–4850, DOI: 10.1002/adma.201100984.

18 F. Wu, J. T. Lee, E. Zhao, B. Zhang and G. Yushin, Graphene–Li$_2$ S–Carbon Nanocomposite for Lithium–Sulfur Batteries, *ACS Nano*, 2016, **10**(1), 1333–1340, DOI: 10.1021/acsnano.5b06716.

19 G. Chen, W. Zhong, Y. Li, Q. Deng, X. Ou, Q. Pan, X. Wang, X. Xiong, C. Yang and M. Liu, Rational Design of TiO–TiO$_2$ Heterostructure/Polypyrrole as a Multifunctional Sulfur Host for Advanced Lithium–Sulfur Batteries, *ACS Appl. Mater. Interfaces*, 2019, **11**(5), 5055–5063, DOI: 10.1021/acsami.8b19501.

20 L. Jiao, C. Zhang, C. Geng, S. Wu, H. Li, W. Lv, Y. Tao, Z. Chen, G. Zhou, J. Li, G. Ling, Y. Wan and Q. Yang, Capture and Catalytic Conversion of Polysulfides by *In Situ* Built TiO$_2$-MXene Heterostructures for Lithium–Sulfur Batteries, *Adv. Energy Mater.*, 2019, **9**(19), 1900219, DOI: 10.1002/aenm.201900219.

21 Y. Wang, R. Zhang, J. Chen, H. Wu, S. Lu, K. Wang, H. Li, C. J. Harris, K. Xi, R. V. Kumar and S. Ding, Enhancing Catalytic Activity of Titanium Oxide in Lithium–Sulfur Batteries by Band Engineering, *Adv. Energy Mater.*, 2019, **9**(24), 1900953, DOI: 10.1002/aenm.201900953.

22 N. Baikalov, N. Serik, S. Kalybekkyzy, I. Kurmanbayeva, Z. Bakenov and A. Mentbayeva, High Mass-Loading Sulfur-Composite Cathode for Lithium-Sulfur Batteries, *Front. Energy Res.*, 2020, **8**, 207, DOI: 10.3389/fenrg.2020.00207.

23 L. P. Zhang, Y. F. Wang, S. Q. Gou and J. H. Zeng, All Inorganic Frameworks of Tin Dioxide Shell as Cathode Material for Lithium Sulfur Batteries with Improved Cycle Performance, *J. Phys. Chem. C*, 2015, **119**(52), 28721–28727, DOI: 10.1021/acs.jpcc.5b08934.

24 X. Liang and L. F. Nazar, *In Situ* Reactive Assembly of Scalable Core–Shell Sulfur–MnO$_2$ Composite Cathodes, *ACS Nano*, 2016, **10**(4), 4192–4198, DOI: 10.1021/acsnano.5b07458.

25 S. Chung and A. Manthiram, A Li$_2$ S-TiS$_2$ -Electrolyte Composite for Stable Li$_2$ S-Based Lithium–Sulfur Batteries, *Adv. Energy Mater.*, 2019, **9**(30), 1901397, DOI: 10.1002/aenm.201901397.

26 M. Chen, W. Xu, S. Jamil, S. Jiang, C. Huang, X. Wang, Y. Wang, H. Shu, K. Xiang and P. Zeng, Multifunctional Heterostructures for Polysulfide Suppression in High-Performance Lithium-Sulfur Cathode, *Small*, 2018, **14**(49), 1803134, DOI: 10.1002/smll.201803134.

27 Z. Cui, J. Yao, T. Mei, S. Zhou, B. Hou, J. Li, J. Li, J. Wang, J. Qian and X. Wang, Strong Lithium Polysulfides Chemical Trapping of TiC-TiO_2/S Composite for Long-Cycle Lithium-Sulfur Batteries, *Electrochim. Acta*, 2019, **298**, 43–51, DOI: 10.1016/j.electacta.2018.12.075.

28 X. Liang, A. Garsuch and L. F. Nazar, Sulfur Cathodes Based on Conductive MXene Nanosheets for High-Performance Lithium–Sulfur Batteries, *Angew. Chem., Int. Ed.*, 2015, **54**(13), 3907–3911, DOI: 10.1002/anie.201410174.

29 Y. Liao, J. Xiang, L. Yuan, Z. Hao, J. Gu, X. Chen, K. Yuan, P. K. Kalambate and Y. Huang, Biomimetic Root-like TiN/C@S Nanofiber as a Freestanding Cathode with High Sulfur Loading for Lithium–Sulfur Batteries, *ACS Appl. Mater. Interfaces*, 2018, **10**(44), 37955–37962, DOI: 10.1021/acsami.8b11118.

30 D.-R. Deng, F. Xue, Y.-J. Jia, J.-C. Ye, C.-D. Bai, M.-S. Zheng and Q.-F. Dong, Co_4 N Nanosheet Assembled Mesoporous Sphere as a Matrix for Ultrahigh Sulfur Content Lithium–Sulfur Batteries, *ACS Nano*, 2017, **11**(6), 6031–6039, DOI: 10.1021/acsnano.7b01945.

31 C. Zhao, Y. Wu, H. Liang, X. Chen, J. Tang and X. Wang, N-Doped Graphene and TiO_2 Supported Manganese and Cerium Oxides on Low-Temperature Selective Catalytic Reduction of NO_x with NH_3, *J. Adv. Ceram.*, 2018, **7**(3), 197–206, DOI: 10.1007/s40145-018-0271-7.

32 H. Rasoulnezhad, G. Hosseinzadeh, R. Hosseinzadeh and N. Ghasemian, Preparation of Transparent Nanostructured N-Doped TiO2 Thin Films by Combination of Sonochemical and CVD Methods with Visible Light Photocatalytic Activity, *J. Adv. Ceram.*, 2018, **7**(3), 185–196, DOI: 10.1007/s40145-018-0270-8.

33 H. Shao, W. Wang, H. Zhang, A. Wang, X. Chen and Y. Huang, Nano-TiO_2 Decorated Carbon Coating on the Separator to Physically and Chemically Suppress the Shuttle Effect for Lithium-Sulfur Battery, *J. Power Sources*, 2018, **378**, 537–545, DOI: 10.1016/j.jpowsour.2017.12.067.

34 C. Zha, D. Wu, T. Zhang, J. Wu and H. Chen, A Facile and Effective Sulfur Loading Method: Direct Drop of Liquid Li_2S_8 on Carbon Coated TiO_2 Nanowire Arrays as Cathode towards Commercializing Lithium-Sulfur Battery, *Energy Storage Mater.*, 2019, **17**, 118–125, DOI: 10.1016/j.ensm.2018.11.020.

35 Z. Wei Seh, W. Li, J. J. Cha, G. Zheng, Y. Yang, M. T. McDowell, P.-C. Hsu and Y. Cui, Sulphur–TiO2 Yolk–Shell Nanoarchitecture with Internal Void Space for Long-Cycle Lithium–Sulphur Batteries, *Nat. Commun.*, 2013, **4**(1), 1331, DOI: 10.1038/ncomms2327.

36 P. Pazhamalai, K. Krishnamoorthy, V. K. Mariappan and S.-J. Kim, Blue TiO_2 Nanosheets as a High-Performance Electrode Material for Supercapacitors, *J. Colloid Interface Sci.*, 2019, **536**, 62–70, DOI: 10.1016/j.jcis.2018.10.031.

37 X. Zhang, T. Yang, J. Liu, C. Hu, S. Gao, Z. Shi, Q. Wu, H. Li, Y. Zhang and Z. Chen, Atomic-Level Catalyst Coupled with Metal Oxide Heterostructure for Promoting Kinetics of Lithium-Sulfur Batteries, *Small*, 2024, **20**(31), 2311086, DOI: 10.1002/smll.202311086.

38 J. Zhu, Y. Liu, L. Zhong, J. Wang, H. Chen, S. Zhao and Y. Qiu, Hybrid TiO-TiO2 Nanoparticle/B-N Co-Doped CNFs Interlayer for Advanced Li S Batteries, *J. Electroanal. Chem.*, 2021, **881**, 114950, DOI: 10.1016/j.jelechem.2020.114950.

39 X. Meng, Z. Chen, S. Hong, L. Jin, H. Liu, C. He, Y. Che, Z. Zhang, J. Yu, Z. Yang and J. Cai, TiO2 Nanotubes Loaded WS_2/MoS_2 to Construct Heterostructures to Accelerate the Conversion of Polysulfide in Lithium–Sulfur Batteries, *Mater. Today Chem.*, 2024, **42**, 102351, DOI: 10.1016/j.mtchem.2024.102351.

40 Y. Chen, W. Tang, J. Ma, B. Ge, X. Wang, Y. Wang, P. Ren and R. Liu, Nickel-Decorated TiO_2 Nanotube Arrays as a Self-Supporting Cathode for Lithium–Sulfur Batteries, *Front. Mater. Sci.*, 2020, **14**(3), 266–274, DOI: 10.1007/s11706-020-0509-5.

41 F. Hilario, V. Roche, R. P. Nogueira and A. M. J. Junior, Influence of Morphology and Crystalline Structure of TiO_2 Nanotubes on Their Electrochemical Properties and Apatite-Forming Ability, *Electrochim. Acta*, 2017, **245**, 337–349, DOI: 10.1016/j.electacta.2017.05.160.

42 F. Riboni, N. T. Nguyen, S. So and P. Schmuki, Aligned Metal Oxide Nanotube Arrays: Key-Aspects of Anodic TiO_2 Nanotube Formation and Properties, *Nanoscale Horiz.*, 2016, **1**(6), 445–466, DOI: 10.1039/C6NH00054A.

43 I. Paramasivam, H. Jha, N. Liu and P. Schmuki, A Review of Photocatalysis Using Self-organized TiO_2 Nanotubes and Other Ordered Oxide Nanostructures, *Small*, 2012, **8**(20), 3073–3103, DOI: 10.1002/smll.201200564.

44 S. Reghunath, D. Pinheiro and S. D. Kr, A Review of Hierarchical Nanostructures of TiO_2: Advances and Applications, *Appl. Surf. Sci. Adv.*, 2021, **3**, 100063, DOI: 10.1016/j.apsadv.2021.100063.

45 T. Appadurai, C. Subramaniyam, R. Kuppusamy, S. Karazhanov and B. Subramanian, Electrochemical Performance of Nitrogen-Doped TiO_2 Nanotubes as Electrode Material for Supercapacitor and Li-Ion Battery, *Molecules*, 2019, **24**(16), 2952, DOI: 10.3390/molecules24162952.

46 Y. Lin, Q. Qian, Z. Chen, P. Dinh Tuan and D. Feng, Fabrication of High Specific Surface Area TiO_2 Nanopowders by Anodization of Porous Titanium, *Electrochem. Commun.*, 2022, **136**, 107234, DOI: 10.1016/j.elecom.2022.107234.

47 J. Liu, Y. Liu, T. Li, L. Liang, S. Wen, Y. Zhang, G. Liu, F. Ren and G. Wang, Efficient Regulation of Polysulfides by Anatase/Bronze TiO_2 Heterostructure/Polypyrrole Composites for High-Performance Lithium-Sulfur Batteries, *Molecules*, 2023, **28**(11), 4286, DOI: 10.3390/molecules28114286.

48 N. Liu, L. Wang, T. Tan, Y. Zhao and Y. Zhang, TiO_2/GO-Coated Functional Separator to Suppress Polysulfide Migration in Lithium–Sulfur Batteries, *Beilstein J. Nanotechnol.*, 2019, **10**, 1726–1736, DOI: 10.3762/bjnano.10.168.

49 X. Mettan, J. Jaćimović, O. S. Barišić, A. Pisoni, I. Batistić, E. Horváth, S. Brown, L. Rossi, P. Szirmai, B. Farkas, H. Berger and L. Forró, Tailoring Thermal Conduction in

Anatase TiO_2, *Commun. Phys.*, 2019, **2**(1), 123, DOI: 10.1038/s42005-019-0224-7.

50 Z. W. Seh, Y. Sun, Q. Zhang and Y. Cui, Designing High-Energy Lithium–Sulfur Batteries, *Chem. Soc. Rev.*, 2016, **45**(20), 5605–5634, DOI: 10.1039/C5CS00410A.

51 Y. Gui, P. Chen, D. Liu, Y. Fan, J. Zhou, J. Zhao, H. Liu, X. Guo, W. Liu and Y. Cheng, TiO2 Nanotube/RGO Modified Separator as an Effective Polysulfide-Barrier for High Electrochemical Performance Li-S Batteries, *J. Alloys Compd.*, 2022, **895**, 162495, DOI: 10.1016/j.jallcom.2021.162495.

52 X. He, H. Hou, X. Yuan, L. Huang, J. Hu, B. Liu, J. Xu, J. Xie, J. Yang, S. Liang and X. Wu, Electrocatalytic Activity of Lithium Polysulfides Adsorbed into Porous TiO_2 Coated MWCNTs Hybrid Structure for Lithium-Sulfur Batteries, *Sci. Rep.*, 2017, **7**(1), 40679, DOI: 10.1038/srep40679.

53 J. Pu, G. Zhu, S. Chang, X. Zhu, Z. Wang and P. Xue, Interfacial Engineering of Ru Nanocluster-Modified TiO_2 Nanotube-Assisted Regulation of Lithium Polysulfide Reactions, *Inorg. Chem.*, 2023, **62**(44), 18307–18314, DOI: 10.1021/acs.inorgchem.3c03163.

54 Z. Barlow, Z. Wei and R. Wang, Boosting Lithium Polysulfide Conversion *via* TiO_2-Supported Niobium Catalyst for Lithium Sulfur Battery, *Mater. Chem. Phys.*, 2024, **314**, 128830, DOI: 10.1016/j.matchemphys.2023.128830.

55 N. Baikalov, I. Rakhimbek, A. Konarov, A. Mentbayeva, Y. Zhang and Z. Bakenov, Catalytic Effects of Ni Nanoparticles Encapsulated in Few-Layer N-Doped Graphene and Supported by N-Doped Graphitic Carbon in Li–S Batteries, *RSC Adv.*, 2023, **13**(14), 9428–9440, DOI: 10.1039/D3RA00891F.

56 I. Rakhimbek, N. Baikalov, A. Konarov, A. Mentbayeva, Y. Zhang and Z. Bakenov, Nickel and Nickel Oxide Nanoparticle-Embedded Functional Carbon Nanofibers for Lithium Sulfur Batteries, *Nanoscale Adv.*, 2024, **6**(2), 578–589, DOI: 10.1039/D3NA00785E.

57 Z. Shen, Z. Zhang, M. Li, Y. Yuan, Y. Zhao, S. Zhang, C. Zhong, J. Zhu, J. Lu and H. Zhang, Rational Design of a Ni_3 $N_{0.85}$ Electrocatalyst to Accelerate Polysulfide Conversion in Lithium–Sulfur Batteries, *ACS Nano*, 2020, **14**(6), 6673–6682, DOI: 10.1021/acsnano.9b09371.

58 J. Liu, X. Wang, T. Gao, W. Yang, Q. Jian, B. Li, L. He and Y. A. Ruan, NiCo Oxide/NiCo Sulfate Hollow Nanowire-Coated Separator: A Versatile Strategy for Polysulfide Trapping and Catalytic Conversion in High-Performance Lithium–Sulfur Batteries, *RSC Adv.*, 2025, **15**(13), 9875–9883, DOI: 10.1039/D5RA00172B.

59 K. Alkanad, A. Hezam, N. Al-Zaqri, M. A. Bajiri, G. Alnaggar, Q. A. Drmosh, H. A. Almukhlifi and L. Neratur Krishnappagowda, One-Step Hydrothermal Synthesis of Anatase TiO_2 Nanotubes for Efficient Photocatalytic CO_2 Reduction, *ACS Omega*, 2022, **7**(43), 38686–38699, DOI: 10.1021/acsomega.2c04211.

60 Y. Bahari Molla Mahaleh, S. K. Sadrnezhaad and D. Hosseini, NiO Nanoparticles Synthesis by Chemical Precipitation and Effect of Applied Surfactant on Distribution of Particle Size, *J. Nanomater.*, 2008, **2008**(1), 470595, DOI: 10.1155/2008/470595.

61 S. Li, X. Chen, F. Hu, R. Zeng, Y. Huang, L. Yuan and J. Xie, Cobalt-Embedded Carbon Nanofiber as Electrocatalyst for Polysulfide Redox Reaction in Lithium Sulfur Batteries, *Electrochim. Acta*, 2019, **304**, 11–19, DOI: 10.1016/j.electacta.2019.02.087.

62 H. Wang, X. Kou, L. Zhang and J. Li, Size-Controlled Synthesis, Microstructure and Magnetic Properties of Ni Nanoparticles, *Mater. Res. Bull.*, 2008, **43**(12), 3529–3536, DOI: 10.1016/j.materresbull.2008.01.012.

63 J. Lynch, C. Giannini, J. K. Cooper, A. Loiudice, I. D. Sharp and R. Buonsanti, Substitutional or Interstitial Site-Selective Nitrogen Doping in TiO_2 Nanostructures, *J. Phys. Chem. C*, 2015, **119**(13), 7443–7452, DOI: 10.1021/jp512775s.

64 H. Zhang, W. Qiu, Y. Zhang, Y. Han, M. Yu, Z. Wang, X. Lu and Y. Tong, Surface Engineering of Carbon Fiber Paper for Efficient Capacitive Energy Storage, *J. Mater. Chem. A*, 2016, **4**(47), 18639–18645, DOI: 10.1039/C6TA08138J.

65 X. Chen, X. Wang and D. Fang, A Review on C1s XPS-Spectra for Some Kinds of Carbon Materials, *Fullerenes, Nanotubes Carbon Nanostruct.*, 2020, **28**(12), 1048–1058, DOI: 10.1080/1536383X.2020.1794851.

66 A. P. Grosvenor, M. C. Biesinger, R. St. C. Smart and N. S. McIntyre, New Interpretations of XPS Spectra of Nickel Metal and Oxides, *Surf. Sci.*, 2006, **600**(9), 1771–1779, DOI: 10.1016/j.susc.2006.01.041.

67 H.-B. Kim and D.-J. Jang, Morphological Variation of Anatase TiO_2 Crystals *via* Formation of Titanium Glycerolate Precursors under Microwave Irradiation, *CrystEngComm*, 2015, **17**(17), 3325–3332, DOI: 10.1039/C5CE00257E.

68 J. Ni, S. Fu, C. Wu, J. Maier, Y. Yu and L. Li, Self-Supported Nanotube Arrays of Sulfur-Doped TiO_2 Enabling Ultrastable and Robust Sodium Storage, *Adv. Mater.*, 2016, **28**(11), 2259–2265, DOI: 10.1002/adma.201504412.

69 L. Zhu, Q. Lu, L. Lv, Y. Wang, Y. Hu, Z. Deng, Z. Lou, Y. Hou and F. Teng, Ligand-Free Rutile and Anatase TiO_2 Nanocrystals as Electron Extraction Layers for High Performance Inverted Polymer Solar Cells, *RSC Adv.*, 2017, **7**(33), 20084–20092, DOI: 10.1039/C7RA00134G.

70 C. Li, X. Liu, L. Zhu, R. Huang, M. Zhao, L. Xu and Y. Qian, Conductive and Polar Titanium Boride as a Sulfur Host for Advanced Lithium–Sulfur Batteries, *Chem. Mater.*, 2018, **30**(20), 6969–6977, DOI: 10.1021/acs.chemmater.8b01352.

71 S. Huang, X. Zhao, Z. Yu, W. Tong and Y. Zhang, Honeycomb Graphite Network Confined in Biphasic TiO_2 Homojunction Nanotubes as the Sulfur Host for Advanced Lithium Sulfur Batteries, *J. Mater. Chem. A*, 2025, **13**(30), 24590–24598, DOI: 10.1039/D5TA04041H.

72 A. Khamrai, S. Ghosh and V. Ganesh, Advances in Accessing Rare Oxidation States of Nickel for Catalytic Innovation, *Chem. Commun.*, 2025, **61**(15), 3037–3060, DOI: 10.1039/D4CC06415A.

73 A. Khamrai, S. Ghosh and V. Ganesh, Advances in Accessing Rare Oxidation States of Nickel for Catalytic Innovation, *Chem. Commun.*, 2025, **61**(15), 3037–3060, DOI: 10.1039/D4CC06415A.

74 M. Chen, X. Zhao, Y. Li, P. Zeng, H. Liu, H. Yu, M. Wu, Z. Li, D. Shao, C. Miao, G. Chen, H. Shu, Y. Pei and X. Wang, Kinetically Elevated Redox Conversion of Polysulfides of Lithium–Sulfur Battery Using a Separator Modified with Transition Metals Coordinated g-C_3N_4 with Carbon-Conjugated, *Chem. Eng. J.*, 2020, **385**, 123905, DOI: 10.1016/j.cej.2019.123905.

75 Y. Liu, D. Han, L. Wang, G. Li, S. Liu and X. Gao, $NiCo_2O_4$ Nanofibers as Carbon-Free Sulfur Immobilizer to Fabricate Sulfur-Based Composite with High Volumetric Capacity for Lithium–Sulfur Battery, *Adv. Energy Mater.*, 2019, **9**(11), 1803477, DOI: 10.1002/aenm.201803477.

76 S. Wang, Y. Wang, Y. Song, X. Jia, J. Yang, Y. Li, J. Liao and H. Song, Immobilizing Polysulfide *via* Multiple Active Sites in $W_{18}O_{49}$ for Li–S Batteries by Oxygen Vacancy Engineering, *Energy Storage Mater.*, 2021, **43**, 422–429, DOI: 10.1016/j.ensm.2021.09.020.

77 K. Xiao, Z. Chen, Z. Liu, L. Zhang, X. Cai, C. Song, Z. Fan, X. Chen, J. Liu and Z. X. Shen, N-Doped Carbon Sheets Arrays Embedded with CoP Nanoparticles as High-Performance Cathode for Li–S Batteries *via* Triple Synergistic Effects, *J. Power Sources*, 2020, **455**, 227959, DOI: 10.1016/j.jpowsour.2020.227959.

78 S. S. Zhang, Liquid Electrolyte Lithium/Sulfur Battery: Fundamental Chemistry, Problems, and Solutions, *J. Power Sources*, 2013, **231**, 153–162, DOI: 10.1016/j.jpowsour.2012.12.102.

79 E. M. Espinoza, J. A. Clark, J. Soliman, J. B. Derr, M. Morales and V. I. Vullev, Practical Aspects of Cyclic Voltammetry: How to Estimate Reduction Potentials When Irreversibility Prevails, *J. Electrochem. Soc.*, 2019, **166**(5), H3175–H3187, DOI: 10.1149/2.0241905jes.

80 J. Wang, L. Jia, J. Zhong, Q. Xiao, C. Wang, K. Zang, H. Liu, H. Zheng, J. Luo, J. Yang, H. Fan, W. Duan, Y. Wu, H. Lin and Y. Zhang, Single-Atom Catalyst Boosts Electrochemical Conversion Reactions in Batteries, *Energy Storage Mater.*, 2019, **18**, 246–252, DOI: 10.1016/j.ensm.2018.09.006.

81 S. Azam, Z. Wei and R. Wang, Adsorption-Catalysis Design with Cerium Oxide Nanorods Supported Nickel–Cobalt-Oxide with Multifunctional Reaction Interfaces for Anchoring Polysulfides and Accelerating Redox Reactions in Lithium Sulfur Battery, *J. Colloid Interface Sci.*, 2023, **635**, 466–480, DOI: 10.1016/j.jcis.2022.12.130.

82 J. Pu, Z. Shen, J. Zheng, W. Wu, C. Zhu, Q. Zhou, H. Zhang and F. Pan, Multifunctional Co3S4@sulfur Nanotubes for Enhanced Lithium-Sulfur Battery Performance, *Nano Energy*, 2017, **37**, 7–14, DOI: 10.1016/j.nanoen.2017.05.009.

83 D. Liu, H. Li, K. Li and M. Zhen, Adsorption, Diffusion and Electrocatalytic Triple Effect from Ultrathin-Walled TiO_2(B) Nanotubes for Lithium–Sulfur Batteries, *J. Taiwan Inst. Chem. Eng.*, 2022, **132**, 104164, DOI: 10.1016/j.jtice.2021.104164.

84 A. Ch. Lazanas and M. I. Prodromidis, Electrochemical Impedance Spectroscopy–A Tutorial, *ACS Meas. Sci. Au*, 2023, **3**(3), 162–193, DOI: 10.1021/acsmeasuresciau.2c00070.

85 A. Manthiram, Y. Fu, S.-H. Chung, C. Zu and Y.-S. Su, Rechargeable Lithium–Sulfur Batteries, *Chem. Rev.*, 2014, **114**(23), 11751–11787, DOI: 10.1021/cr500062v.

86 S. Xu, Y. Zhang, Y. Shi, C. Wang and J. Qiu, Three-Dimensional Macroporous TiO_2-MXene Nanostructure-Based Films for Flexible Freestanding Sulfur Cathodes, *ACS Appl. Nano Mater.*, 2022, **5**(11), 16853–16861, DOI: 10.1021/acsanm.2c03796.

87 Z. Qiu, Y. Zhang, X. Huang, J. Duan, D. Wang, G. P. Nayaka, X. Li and P. Dong, Beneficial Effect of Incorporating Ni-Rich Oxide and Layered over-Lithiated Oxide into High-Energy-Density Cathode Materials for Lithium-Ion Batteries, *J. Power Sources*, 2018, **400**, 341–349, DOI: 10.1016/j.jpowsour.2018.08.041.

88 H. Wu, Y. Li, J. Ren, D. Rao, Q. Zheng, L. Zhou and D. Lin, CNT-Assembled Dodecahedra Core@nickel Hydroxide Nanosheet Shell Enabled Sulfur Cathode for High-Performance Lithium-Sulfur Batteries, *Nano Energy*, 2019, **55**, 82–92, DOI: 10.1016/j.nanoen.2018.10.061.

89 A. Chen, W. Liu, H. Hu, T. Chen, B. Ling and K. Liu, Three-Dimensional TiO2-B Nanotubes/Carbon Nanotubes Intertwined Network as Sulfur Hosts for High Performance Lithium–sulfur Batteries, *J. Power Sources*, 2018, **400**, 23–30, DOI: 10.1016/j.jpowsour.2018.08.004.

90 H.-J. Chen, P. Lu, R. Guo and Q. Sun, Nickel Nanoparticles Embedded N-Doped Mesoporous Graphitized Carbon Nanoflake as Multifunctional Sulfur Host for High-Performance Lithium–Sulfur Batteries, *J. Alloys Compd.*, 2022, **921**, 166144, DOI: 10.1016/j.jallcom.2022.166144.

91 Y. Jiang, Y. Deng, B. Zhang, W. Hua, X. Wang, Q. Qi, Q. Lin and W. Lv, An Interlayer Composed of a Porous Carbon Sheet Embedded with TiO_2 Nanoparticles for Stable and High Rate Lithium–Sulfur Batteries, *Nanoscale*, 2020, **12**(23), 12308–12316, DOI: 10.1039/D0NR02607G.

92 X. Shang, P. Guo, T. Qin, M. Liu, M. Lv, D. Liu and D. He, Sulfur Immobilizer by Nanoscale TiO_2 Trapper Deposited on Hierarchical Porous Carbon and Graphene for Cathodes of Lithium–Sulfur Batteries, *Adv. Mater. Interfaces*, 2018, **5**(7), 1701602, DOI: 10.1002/admi.201701602.

93 Y. Hou, J. Kullgren, L. Han, P. Qian, W. Yuan, J. Liu, H. Xie and J. Zhu, NiO-Ni2P/C3N4 Heterostructures with Synergistic Adsorption-Electrocatalysis Functions for Suppressing Polysulfide Shuttle Effect in Lithium Sulfur Batteries, *J. Colloid Interface Sci.*, 2025, **697**, 137972, DOI: 10.1016/j.jcis.2025.137972.

94 J. Lu, M. Zhu, M. Kim, A. He, C. Wang, T. H. Kim and S. H. Lee, Catalytic Nickel Nanoparticles Embedded on ZIF-8 Backbone for Accelerating Polysulfide Conversion in Lithium–Sulfur Batteries, *J. Power Sources*, 2025, **647**, 237269, DOI: 10.1016/j.jpowsour.2025.237269.

95 Y. Liu, M. Li, R. Yang, Q. Meng, D. Baek, H. Lim, J. Kim and J. Ahn, Immobilization and Catalytic Conversion of Polysulfide by *In Situ* Generated Nickel in Hollow Carbon Fibers for High-Rate Lithium–Sulfur Batteries, *ChemSusChem*, 2025, **18**(2), e202401178, DOI: 10.1002/cssc.202401178.

96 H. Zhang, D. Tian, Z. Zhao, X. Liu, Y.-N. Hou, Y. Tang, J. Liang, Z. Zhang, X. Wang and J. Qiu, Cobalt Nitride Nanoparticles Embedded in Porous Carbon Nanosheet Arrays Propelling Polysulfides Conversion for Highly Stable Lithium–Sulfur Batteries, *Energy Storage Mater.*, 2019, **21**, 210–218, DOI: 10.1016/j.ensm.2018.12.005.

97 J. Zhou, D. Zhang, T. Wan, X. Wang, G. Liu, Y. Zhang, J. Li and Y. Wang, Pomegranate-like Conductive Spherical Composite as Multifunctional Cathode for High-Performance Lithium-Sulfur Battery, *J. Alloys Compd.*, 2021, **855**, 157382, DOI: 10.1016/j.jallcom.2020.157382.

98 M. A. Al-Tahan, Y. Dong, R. Zhang, Y. Zhang and J. Zhang, Understanding the High-Performance $Fe(OH)_3$@GO Nanoarchitecture as Effective Sulfur Hosts for the High Capacity of Lithium–Sulfur Batteries, *Appl. Surf. Sci.*, 2021, **538**, 148032, DOI: 10.1016/j.apsusc.2020.148032.

99 K. Xie, Y. Han, W. Wei, H. Yu, C. Zhang, J.-G. Wang, W. Lu and B. Wei, Fabrication of a Novel TiO_2/S Composite Cathode for High Performance Lithium–Sulfur Batteries, *RSC Adv.*, 2015, **5**(94), 77348–77353, DOI: 10.1039/C5RA13823J.